Room-Temperature Apo Structure of Human SIRT2 Solved by X-ray

Crystallography and Its Application in Targeted Cancer Drug Development

by

Seyide Seda Paydos

A Dissertation Submitted to the
Graduate School of Sciences and Engineering

in Partial Fulfillment of the Requirements for

the Degree of

Master of Science

In

Molecular Biology and Genetics

July 11, 2025

Room-Temperature Apo Structure of Human SIRT2 Solved by X-ray

Crystallography and Its Application in Targeted Cancer Drug Development

Koç University

Graduate School of Sciences and Engineering

This is to certify that I have examined this copy of a master's thesis by

Seyide Seda Paydos

and have found that it is complete and satisfactory in all respects,
and that any and all revisions required by the final
examining committee have been made.

Advisors:

Asst. Prof. Hasan Demirci (Advisor)

Assoc. Prof. Halil İbrahim Çiftçi (Co-Advisor)

Committee Members:

Asst. Prof. Onur Öztaş

Assoc. Prof. Belgin Sever

Date: 11 July 2025

ABSTRACT

Room-Temperature Apo Structure of Human SIRT2 Solved by X-ray Crystallography and Its Application in Targeted Cancer Drug Development

Seyide Seda Paydos

Master of Science in Molecular Biology and Genetics

July 11, 2025

Sirtuins are a family of NAD^+-dependent deacetylases that regulate gene expression through histone modification and play crucial roles in cellular processes such as stress response, metabolism, aging, and cancer. Among the seven mammalian isoforms (SIRT1–SIRT7), SIRT2 is unique in its ability to function in both the nucleus and cytoplasm, modulating the acetylation status of key regulatory proteins involved in cell cycle control. This regulation implicates SIRT2 in tumorigenesis and the development of drug resistance. In this study, we report the ambient-temperature apo structure of human SIRT2 determined by X-ray crystallography, providing a physiologically relevant model that captures the enzyme's intrinsic conformational flexibility under near-native conditions. Compared to traditional cryogenic structures, the room-temperature data reveal a narrower, likely inactive conformation of the inhibitor binding pocket and active site which undergoes expansion upon ligand binding. Comparative structural analyses identify key residues critical for ligand interactions and highlight the dynamic interplay between protein flexibility, temperature, and ligand presence. These insights significantly deepen our understanding of SIRT2's functional mechanism and are vital for the rational design of selective inhibitors. By integrating ambient-temperature structural data, this work establishes a foundation for structure-based drug discovery targeting SIRT2, advancing efforts in the development of targeted cancer therapeutics. Moreover, these findings emphasize the importance of considering physiological flexibility in proteins to improve the effectiveness and specificity of novel drugs.

ÖZETÇE

İnsan Apo SIRT2 Yapısının X-ışını Kristalografisi ile Oda Sıcaklığında Çözülmesi ve Hedefe Yönelik Kanser İlaç Geliştirilmesinde Uygulaması

Seyide Seda Paydos

Moleküler Biyoloji ve Genetik Yüksek Lisans

11 Temmuz 2025

Sirtuinler, histon proteinlerini modifiye ederek gen ifadesini düzenleyen ve stres yanıtı, metabolizma, yaşlanma ve kanser gibi hayati süreçlerde rol oynayan NAD^+-bağımlı deasetilazlar ailesidir. Yedi memeli izoformu (SIRT1–SIRT7) arasında SIRT2 hem çekirdek hem de sitoplazmada işlev görerek hücre döngüsünün düzenlenmesinde anahtar rol oynayan proteinlerin asetilasyon durumunu modüle eder. Bu işlevi nedeniyle SIRT2 tümör oluşumu ve ilaç direnci süreçlerinde önemli bir role sahiptir. Bu çalışmada, insan SIRT2'nin oda sıcaklığında apo yapısı X-ışını kristalografisi yöntemiyle çözümlenmiş ve enzimin doğal ortamına daha uygun, konformasyonel esnekliğini yansıtan bir model sunulmuştur. Kriyojenik (düşük sıcaklıkta) yapılarla karşılaştırıldığında, oda sıcaklığında elde edilen yapının inhibitör bağlanma cebinde ve aktif bölgede daha dar ve muhtemelen inaktif bir konformasyon sergilediği görülmüş, bu bölge ligand bağlandığında belirgin şekilde genişlemektedir. Yapısal karşılaştırmalar, ligand etkileşiminde rol oynayan kritik kalıntıları ortaya koymakta ve protein esnekliği, sıcaklık değişimi ile ligand varlığı arasındaki dinamik ilişkinin önemini vurgulamaktadır. Bu bulgular, SIRT2'nin moleküler mekanizmasının daha derinlemesine anlaşılmasını sağlamakta ve seçici inhibitörlerin rasyonel tasarımı için temel teşkil etmektedir. Oda sıcaklığında elde edilen bu yapısal verilerin yapıya dayalı ilaç tasarımına entegrasyonu, SIRT2'yi hedef alan kanser terapileri için sağlam ve güvenilir bir zemin oluşturmaktadır. Ayrıca bu çalışma, proteinlerin fizyolojik koşullar altında sergilediği doğal esnekliğin göz önünde bulundurulmasının, etkili ve spesifik ilaç geliştirme süreçlerinde ne denli kritik olduğunu göstermektedir.

ACKNOWLEDGEMENTS

I would like to extend my heartfelt gratitude to my thesis advisor, Assistant Professor Hasan Demirci, as well as Associate Professors Halil İbrahim Çiftçi and Belgin Sever, for their invaluable guidance and support throughout this project.

I am sincerely thankful to TÜBİTAK for funding and supporting my project (No: 122Z047), titled *"SİRT2 Protein-İnhibitör Komplekslerinin Yapısal Dinamik Çalışmaları."*

I am deeply grateful to Haluk Çetinok, Ayça İrgit, and Eda Topalan for their unwavering encouragement and companionship, which made this journey all the more meaningful. Their friendship and enduring support have been a vital source of strength through both challenges and triumphs.

I also wish to express my profound gratitude to my best friends, Melis Yılmaz and Eylül Buse Küçük, whose support has meant more than words can express.

Finally, I owe my deepest appreciation to my family Yeşim, Sedat, and Şener Deniz Paydos whose love, patience, and sacrifices have made the realization of this dream possible.

TABLE OF CONTENTS

LIST OF TABLES

LIST OF FIGURES

ABBREVIATIONS

Å	Angstrom
α	Alpha
β	Beta
γ	Gamma
µg	Microgram
µL	Microliter
°K	Kelvin
Da	Dalton
kDa	Kilodalton
L	Liter
mg	Milligram
M	Molar
mM	Millimolar
min^{-1}	Per Minute
NTA	Nitrilotriacetic Acid
Ni-NTA	Nickel-Nitrilotriacetic Acid
NAD^+	Nicotinamide Adenine Dinucleotide
OD	Optical Density
PDB	Protein Data Bank
RMSD	Root Mean Square Deviation
ROS	Reactive Oxygen Species
rpm	Revolutions Per Minute
SDS-PAGE	Sodium Dodecyl Sulfate Polyacrylamide Gel Electrophoresis
Tris	Tris(hydroxymethyl)aminomethane
SIRT	Sirtuin
SIRT2	Sirtuin 2
WT	Wild-Type
HCl	Hydrochloric Acid
Zn^{2+}	Zinc Ion
IPTG	Isopropyl β-D-1-thiogalactopyranoside
His-tag	Histidine Tag
E. coli	*Escherichia coli*

Chapter 1:

INTRODUCTION

1.1 The Sirtuin Family and Biological Roles of SIRT2

The sirtuin (SIRT) family consists of seven members of class III histone deacetylases. They all contain a conserved NAD^+-dependent catalytic core. Variations in their N- and C-terminal regions regulates their subcellular localization and specific functions (Wu et al., 2022). In humans, this family includes SIRT1 through SIRT7 each function in vital cellular functions such as metabolic regulation, DNA repair, stress responses, and transcriptional control (Sarikhani et al., 2018; Chen et al., 2020). SIRT1, SIRT6, and SIRT7 are mainly nuclear. SIRT2 locates primarily in the cytoplasm which translocate to nucleus and mitochondria. SIRT3 to SIRT5 are localized to mitochondria. Among these, SIRT1 to SIRT3 show strong deacetylase activity (Houtkooper et al., 2012). In contrast to SIRT4 through SIRT7 which display either minimal or undetectable enzymatic activity, SIRT4 has ADP-ribosyltransferase activity (Michishita et al., 2005). SIRT2 exhibits both deacetylase and demyristoylase activity in the mammalian cytoplasm particularly, and its deletion is linked to genomic instability and oncogenesis.

SIRT2 has attracted significant scientific interest due to its unique characteristics and widespread tissue distribution and predominant expression observed in the brain. Its subcellular localization is shown as dynamic however, it is primarily localized in the cytoplasm and translocation into the nucleus and mitochondria was shown (Garmendia-Berges et al., 2023). This translocation enables SIRT2 to participation in diverse cellular processes including cytoskeletal stabilization, DNA repair, gene transcription, autophagy, myelin formation, and inflammation regulation (Sola-Sevilla et al., 2023). Moreover, the presence of lysine acyl modifications on target proteins suggests a role in modulating essential cellular functions (Zhao, Guo, & Li, 2022). While yeast sirtuins regulate epigenetic gene silencing and suppression of ribosomal DNA recombination, human sirtuins including SIRT2 function as intracellular regulatory proteins with mono-ADP-ribosyltransferase and deacetylase activities (Wu et al., 2022). With its enzymatic

properties, SIRT2 is identified as a promising pharmacological target. However, the unpredictable effects resulting from its modulation are raising serious safety concerns. The existence of multiple isoforms and polymorphisms also complicates the interpretation of its biological functions and varying responses to inhibitors.

1.2 The General Roles of SIRT2 in Various Diseases

SIRT2 is involved in various diseases including cancer, age-related conditions, and genomic instability. It functions as an NAD^+-dependent deacetylase and regulates essential cellular processes such as cell cycle, DNA repair, metabolic regulation, and inflammatory responses (Sarikhani et al., 2018; Chen et al., 2020). In cancer, SIRT2 has a dual role as a tumor suppressor or an oncogene depending on the type of cancer and the cellular environment (Chen et al., 2020). SIRT2 also modulates the fundamental proteins that control the cell cycle and apoptosis. Through this regulation, it affects the proliferation and survival of cancer cells. In aging, SIRT2 modulate cellular senescence by controlling the acetylation of proteins that are involved in DNA repair and cell cycle progression (Zhao, Guo, & Li, 2022). The loss of SIRT2 activity is also linked to increased susceptibility to age-related diseases such as Alzheimer's disease and cardiovascular conditions (Zhu et al., 2022). Accordingly, targeting SIRT2 for therapeutic purposes can potentially treat a wide variety of diseases by modulating its activity

1.2.1 Aging

Aging is a complex and gradual deterioration of physiological functions characterized by genomic instability, shortening of telomeres, and epigenetic changes (Wu et al., 2022). SIRT2 is frequently linked to aging and lifespan regulation, and it is proposed to play a key role in modulating age-related diseases (Garmendia-Berges et al., 2023). In yeast, integration of extra copies of Sir2 extends lifespan by up to 30% and deletion of this gene shortens life span by about 50% (Wang et al. 2014). Specifically, SIRT2 overexpression was shown to delay systemic aging in mice by upregulating BubR1 which is a mitotic checkpoint kinase. Upregulation of BubR1 reverses reproductive aging by influencing signaling pathways such as LKB1–AMPK (Sarikhani et al., 2018; North et al., 2014). In the nervous system, SIRT2 supports white matter development and remyelination during aging which indicate a role in reducing age-associated degeneration (Lu et al., 2023). On the other hand, many studies report age-related changes in SIRT2 in

animal models but findings conflict on whether it rises or falls with age, if the effects are beneficial or harmful, and the exact link remains unclear (Garmendia-Berges et al., 2023). Due to its role in aging and conflicting findings, further research is needed to clarify SIRT2's function in age-related decline and its therapeutic potential.

1.2.2 Neurodegenerative Diseases

SIRT2 is highly expressed in mature oligodendrocytes (OLs) but is absent in neurons (Chamberlain et al., 2021). OLs increase axonal mitochondrial ATP production through a transcellular signaling mechanism that modulates the acetylation status of fundamental mitochondrial proteins. Particularly, introducing SIRT2 exogenously into neurons is shown to increase axonal ATP levels which emphasize its potential role in energy metabolism (Chamberlain et al., 2021). Although pharmacological inhibition of SIRT2 offers a promising therapeutic approach for various neurodegenerative diseases, potential peripheral side effects must be carefully assessed (Sola-Sevilla et al., 2023).

Alzheimer's Disease (AD)

Alzheimer's disease (AD), an age-related neurodegenerative disorder, is characterized by amyloid-beta (Aβ) deposition and neurofibrillary tangles (Tailor et al., 2019). Among the sirtuins, SIRT1 and SIRT2 are the most abundant in the brain and have been implicated in the pathogenesis of AD, Parkinson's disease (PD), and Huntington's disease (HD) (Wu et al., 2022). While SIRT1 activation is generally considered neuroprotective, SIRT2 upregulation exerts detrimental effects on neuronal health. Recent studies have highlighted the role of SIRT2 in neurodegenerative diseases, particularly its impact on tau phosphorylation and mitochondrial function. Elevated SIRT2 levels have been shown to induce tau hyperphosphorylation via ERK activation in Neuro2a and Neuro2a-P301L cells, especially under conditions of insulin depletion or interleukin-6 (IL-6) treatment (Zhou et al., 2022). The amyloid precursor protein (APP), a type I transmembrane glycoprotein, undergoes extensive post-translational modifications during its transport through the secretory pathway. Acetylation of APP promotes its non-amyloidogenic processing. SIRT1 and SIRT2 jointly regulate the balance between APP acetylation and deacetylation; SIRT2 removes acetyl groups from APP, whereas SIRT1 prevents SIRT2 from binding to APP (Li et al., 2023). In aging and AD, a decline in protective SIRT1 levels coupled with an increase in harmful SIRT2

levels results in reduced APP acetylation, favoring amyloidogenic processing. Additionally, beyond blocking SIRT2 binding, SIRT1 may enhance APP acetylation through a catalytically independent mechanism, potentially affecting APP trafficking and localization. These findings suggest that targeting the interplay between SIRT1 and SIRT2 could offer new therapeutic strategies for AD (Li et al., 2023).

Huntington's Disease (HD)

Huntington's disease (HD) is an inherited neurodegenerative disorder characterized by motor impairments resulting from an abnormal expansion of CAG repeats in the huntingtin (HTT) gene (Ajitkumar, Lui, & De Jesus, 2025). This mutation leads to protein aggregation and mitochondrial dysfunction. Specifically, it disrupts the normal distribution of dynamin-related protein 1 (Drp1) that results in excessive mitochondrial fragmentation and synaptic degeneration (Wu et al., 2022). Multiple studies suggest that inhibiting SIRT2 can reduce HTT-related toxicity. For instance, the SIRT2 inhibitor AK1 modulates cholesterol metabolism in striatal neurons and prevents neuronal loss in frontotemporal dementia mouse models when injected into the hippocampus (Spiegelman et al., 2018). Another selective SIRT2 inhibitor 33i, influences neuroinflammatory signaling and glutamate receptor function in early senescence-accelerated mice which suggests its potential to prevent age-related neurodegeneration and cognitive decline. Additionally, AGK2 which is a well-known SIRT2 inhibitor, demonstrates neuroprotective effects in ischemic stroke models by downregulating the AKT/FOXO3a/MAPK signaling pathways (Manjula et al., 2021; Sola-Sevilla et al., 2023).

Parkinson's Disease (PD)

In Parkinson's disease (PD), SIRT2 plays an essential role in regulating the aggregation and toxicity of α-synuclein. SIRT2 deacetylates specific lysine residues on α-synuclein which affects how the protein aggregates. Inhibiting SIRT2 is shown to lower α-synuclein toxicity and improve neuronal health (Manjula et al., 2021). SIRT2 inhibitors such as AGK2 reduce neuronal inflammation and brain injury caused by lipopolysaccharide exposure. Another inhibitor AK7, is shown to provide protective effects in several neurodegenerative conditions including both HD and PD (Manjula et al., 2021; Chamberlain et al., 2021). Both genetic and pharmacological inhibition of SIRT2 improve neurological and behavioral outcomes in aged mouse models of PD.

These effects are partly due to enhanced microtubule stability and increased autophagy which help removal of toxic protein aggregates and support cell survival (Manjula et al., 2021).

1.2.3 Infectious Diseases

SIRT2 is shown to participate in antiviral defense and immune modulation. Specifically, SIRT2 and HDAC6 were shown to inhibit the fusion of viral inclusion bodies (Wan et al., 2021). Moreover, SIRT2 expression is increased during infection with all dengue virus (DENV) serotypes and Zika virus. Overexpression of SIRT2 promotes DENV2 replication, while its knockdown inhibits it. Inhibitors like Tenovin-1 reduce DENV propagation by increasing p53 levels and inducing cell death, whereas resveratrol enhances viral replication. Although SIRT2 plays a key role in dengue infection, the exact mechanisms remain unclear and need further study (Wan et al., 2021). These findings suggest SIRT2 as a potential host factor exploited by viruses to facilitate their life cycle and as a viable target for host-directed antiviral therapies.

Besides its role in viral infections, SIRT2 also regulates immune cell metabolism, especially in tumor-infiltrating lymphocytes (TILs). SIRT2 suppresses T cell metabolic activity by reducing the expression of key enzymes involved in glycolysis and oxidative phosphorylation (Hamaidi et al., 2020). Higher SIRT2 levels in TILs are linked to weaker T cell effector functions and poorer outcomes in adoptive TIL therapy for advanced non-small cell lung cancer (Zheng et al., 2021). This is caused by SIRT2 deacetylation of important metabolic regulators like c-Myc which reprogram T cell metabolism and reduce their ability to kill cancer cells (Zheng et al., 2021, Hamaidi et al., 2020). Therefore, targeting SIRT2 could help restore exhausted T cells and improve the effectiveness of cancer immunotherapies especially in tumors with immunosuppressive environments.

1.3 Molecular Mechanisms and Clinical Relevance of SIRT2 in Cancer

SIRT2 regulates various biological processes including aging, metabolism, apoptosis, gene transcription, and inflammation which are critically involved in carcinogenesis initiation and progression. SIRT2 exhibits dual roles in cancer functioning

as an oncogene in certain types (Sarikhani et al., 2018; Ramakrishnan et al., 2014) while functioning as a tumor suppressor in others. These opposing functions rise from its varied biological activities such as its ability to either promote or inhibit cell cycle progression and its modulatory effects on the tumor.

During the cell cycle, SIRT2 predominantly resides in the cytoplasm during interphase but translocates to the nucleus during the G2/M transition where it regulates chromosomal condensation (Garmendia-Berges et al., 2023). In mitosis, SIRT2 interacts with the mitotic spindle and centrosomes to support proper progression. For example, SIRT2 promotes degradation of Aurora A kinase via activation of the anaphase-promoting complex/cyclosome (APC/C) that inhibits cancer cell growth and ensuring mitotic control (Ramakrishnan et al., 2014). Beyond cell cycle regulation, SIRT2 influences the tumor microenvironment by affecting tumor invasion, metastasis, and cellular metabolism, which can facilitate tumor progression (Chen et al., 2020). It also suppresses tumor growth through inhibition of fibroblast activity and angiogenesis, demonstrating a context-dependent role (Yang, Chen, & Hu, 2022)

1.4 The General Promoter and Suppressor Role of SIRT2 in Various Cancers

SIRT2 exhibits a dual function in cancer acting either as a tumor suppressor or an oncogene depending on the cellular context and targets involved (Chen et al., 2020). As a tumor suppressor, SIRT2 deacetylates key proteins such as IDH1, reducing reactive oxygen species (ROS) and inhibiting metastatic signaling in colorectal cancer (Wang et al., 2020). It also stabilizes mitotic checkpoint protein BubR1 to maintain chromosomal integrity (Zhang, Shi, & Han, 2023) and promotes DNA repair by facilitating BRCA1-BARD1 heterodimerization (Minten et al., 2021). Conversely, SIRT2 can act as an oncogene by regulating metabolism and signaling pathways that support tumor growth including modulation of glycolysis and glutaminolysis in T-cells and influencing Wnt/β-catenin signaling in a tissue-specific manner (Hamaidi et al. 2020; Dludla et al., 2023). Overall, SIRT2's complex and sometimes opposing roles highlight its context-dependent impact on cancer progression and suppression.

1.4.1 SIRT2 in Tumor Progression and the Tumor Microenvironment

SIRT2 plays a significant and context-dependent role in tumor invasion and metastasis by modulating the tumor microenvironment (TME). It promotes tumor progression by altering extracellular pH, enhancing cellular energy metabolism, and regulating immune evasion (Chen, Huang, & Hu, 2020). Conversely, SIRT2 can suppress tumorigenesis by inhibiting fibroblast activity and angiogenesis (Yang, Chen, & Hu, 2022). Within the metabolically challenging TME, cancer cells compete with T cells for nutrients which inpairs T cell function.

1.4.2 SIRT2 and T Cell Metabolic Regulation in the TME

SIRT2 acts as a metabolic checkpoint during T-cell activation by suppressing glycolysis and glutaminolysis, thereby limiting T cell proliferation (Hamaidi et al., 2020). In memory T cells, SIRT2 dissociates from fatty acid oxidation (FAO) enzymes that enables a metabolic shift toward FAO during quiescence. SIRT2-deficient T cells exhibit enhanced glycolysis and glutaminolysis that increase their metabolic competitiveness in the TME. Additionally, CD8+ tumor-infiltrating lymphocytes (TILs) upregulate FAO to continue functioning under hypoglycemic conditions. Inhibition of SIRT2 shifts T cells into a hypermetabolic state, improving their antitumor functions and enabling them to overcome the metabolic challenges of the tumor microenvironment (Hamaidi et al., 2020). Consequently, targeting SIRT2 in immunotherapy could enhance the survival and effectiveness of tumor-infiltrating lymphocytes (TILs) and CAR T cells.

1.4.3 Specific Cancer Types

Pancreatic Cancer

Numerous studies have shown that beyond its dual role as an oncogene and tumor suppressor in pancreatic cancer, SIRT2 contributes to cell cycle regulation, maintenance of genomic stability, and modulation of the tumor microenvironment and inflammatory processes. Its atypical expression in both benign and malignant pancreatic tissues suggests that SIRT2 may be a central regulator in pancreatic tumorigenesis (Isohookana et al., 2018). The F-box protein FBXO31, functioning as a substrate recognition

component of the SCF (SKP/Cullin/F-box protein) class E3 ubiquitin ligase complex, facilitates the ubiquitination and degradation of target proteins (Skaar et al., 2018; Senft et al., 2018). Recognized as a tumor suppressor in prostate and breast cancers, FBXO31 is located within a loss of heterozygosity region at chromosome 16q24.3 (Santra et al., 2009). However, some studies report that FBXO31 acts as an oncogene, promoting tumor progression in esophageal and lung cancers (Li et al., 2019; Liu et al., 2018; Huang et al., 2015). In the context of pancreatic cancer, FBXO31 enhances tumor growth and cellular motility, correlating with poor patient survival. Chen et al. demonstrated that FBXO31 reduces SIRT2 protein levels through ubiquitination without affecting its mRNA expression. As SIRT2 inhibits invasion and proliferation of pancreatic cancer cells, its loss leads to increased tumor growth in vivo. Furthermore, METTL3/METTL14-mediated m6A modification upregulates FBXO31 expression while downregulating SIRT2 in pancreatic tumors. METTL3 promotes tumor development by enhancing the m6A methylation of FBXO31, which is dependent on YTHDF1-mediated translational regulation. These findings highlight the role of the METTL3-FBXO31-SIRT2 axis in pancreatic cancer development and suggest novel therapeutic opportunities (Chen et al., 2024).

Another study reports that SIRT2 expression is increased in pancreatic cancer cell lines such as MiaPaca-2 via upregulation by c-Myc. The oncoproteins c-Myc and N-Myc, which are key regulators of cellular proliferation, are stabilized by elevated SIRT2 levels (Liu et al., 2013). Additionally, SIRT2 enhances the activity and stability of the LDH-A (lactate dehydrogenase A) enzyme by deacetylating its K5 residue. LDH-A supports cancer cell migration, survival, and energy metabolism (Zhao et al., 2013). On the other hand, SIRT2 depletion in KRAS mutant mice has been shown to promote tumor growth and enhance KRAS signaling. SIRT2 modulates the acetylation of the KRAS oncoprotein, thereby influencing KRAS activity and its downstream pathways, including RAF/MEK/ERK and PI3K/AKT (Song et al., 2016). Increased tumor aggressiveness and inflammatory responses have been observed in SIRT2-deficient KrasG12D mutant mice, suggesting a tumor-suppressive function for SIRT2 in this genetic context (Quan et al., 2018). These contrasting findings underline the complexity of SIRT2's role in pancreatic cancer and the need for further investigation. Importantly, novel pharmacological inhibitors of SIRT2, such as NPD11033 and fluvastatin sodium, have shown efficacy in

reducing tumor growth by blocking SIRT2 deacetylase activity (Kudo et al., 2018; Yang et al., 2024).

Glioma

Gliomas, including glioblastoma (GBM), are aggressive brain tumors with limited treatment options and poor patient outcomes (Kunadis et al., 2021). Recent research has highlighted the importance of epigenetic regulators in glioma progression and therapy resistance. Among these, SIRT2 has emerged as a critical modulator of chromatin dynamics and tumor suppressor pathways, making it a promising therapeutic target.

SIRT2 has been identified as a key regulator in glioblastoma (GBM) and ATRX-deficient gliomas, making it a potential therapeutic target. Its upregulation in ATRX-deficient gliomas is linked to poor prognosis (Turcan, 2023). SIRT2 promotes chromatin compaction by deacetylating histones H4K16 and H3K27, repressing genes involved in senescence and apoptosis. Inhibitors such as AGK2, AK7, and TH have been shown to reduce tumor cell migration, alter gene expression, and induce senescence in ATRX-deficient glioma cells (Malgulwar et al., 2023). In vivo, AK7 treatment increased H4K16 acetylation, reduced H3K27me3, and suppressed tumor growth while prolonging survival (Malgulwar et al., 2023; Turcan, 2023).

Beyond ATRX-deficient gliomas, SIRT2 also contributes to GBM progression through the regulation of tumor suppressor pathways. Genome-wide studies have frequently identified disruptions in the p53, RB, and RTK signaling pathways in GBM; however, the underlying molecular drivers remain only partially defined (Funato et al., 2018). Recent evidence indicates that SIRT2 promotes oncogenesis by deacetylating the tumor suppressor p73 (structurally related to p53) at its C-terminal lysines, impairing its ability to induce apoptosis and cell cycle arrest. This modification enables GBM cells to evade growth suppression and sustain proliferation. Importantly, SIRT2 inhibition with AK7 was shown to restore p73 function, leading to enhanced apoptosis and reduced GBM cell viability (Funato et al., 2018).

Furthermore, SIRT2 overexpression has been shown to suppress glioma cell proliferation and induce apoptosis by downregulating miR-21 through the SIRT2–NF-

κB–miR-21 axis. This effect is mediated via deacetylation of p65, which blocks its binding to the miR-21 promoter and reduces miR-21 transcription. These findings support the therapeutic relevance of SIRT2 modulation in glioma biology.

Overall, SIRT2 inhibition offers a promising therapeutic strategy for gliomas, particularly in the context of ATRX mutations or p73 dysfunction, by disrupting chromatin structure, inducing cellular senescence, and reactivating tumor suppressor pathways. Future research should further explore combination therapies and elucidate the broader role of SIRT2 in tumor biology to optimize its therapeutic potential.

1.5 SIRT2 Inhibitors and Their Therapeutic Potential

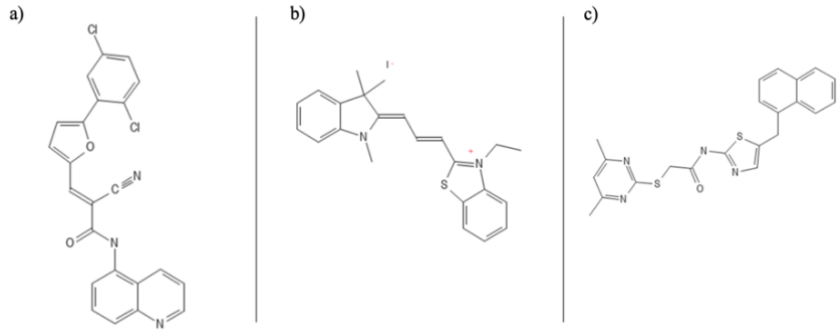

Figure 1.1: . Chemical structures of SIRT2 inhibitors.

a) AGK2, b) AC-93253, and c) SirReal2.

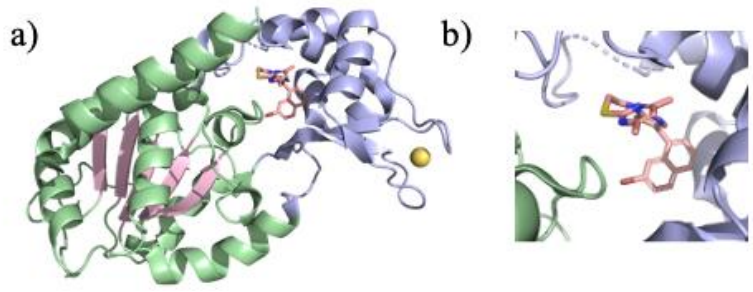

Figure 1.2: Structural representation of the SIRT2-SirReal2 complex

(a) overall structure highlighting the binding of SirReal2 to SIRT2, (b) detailed view of the SirReal2 binding pocket within SIRT2.

SIRT2 inhibitors are compounds developed to specifically block the enzymatic activity of SIRT2 which regulates various cellular functions such as cell cycle progression, metabolism, oxidative stress response, and neuroprotection (Sarikhani et al., 2018; Chen et al., 2020). By inhibiting SIRT2's deacetylase function, these molecules alter the acetylation status of substrates like α-tubulin and histone H4 at lysine 16, affecting microtubule stability, chromatin organization, and gene expression (Turcan, 2024). Due to SIRT2's diverse roles, SIRT2 inhibitors have therapeutic potential across diseases including neurodegenerative disorders, inflammatory conditions, and cancer. Several SIRT2 inhibitors are characterized for their therapeutic effects.

AGK2 is an early and well-studied inhibitor showing neuroprotective and anticancer activity by blocking SIRT2-mediated deacetylation (Malgulwar et al., 2023; Yang et al., 2018). SirReal2 is significant for its high specificity that targets an allosteric site unique to SIRT which minimizes off-target effects (Roshdy et al., 2021). AC-93253 exhibits strong antiproliferative effects in cancer cells (Hu et al., 2014). AK7 is shown to be effective in glioma by inducing senescence through increased histone acetylation and chromatin remodeling (Turcan, 2024).

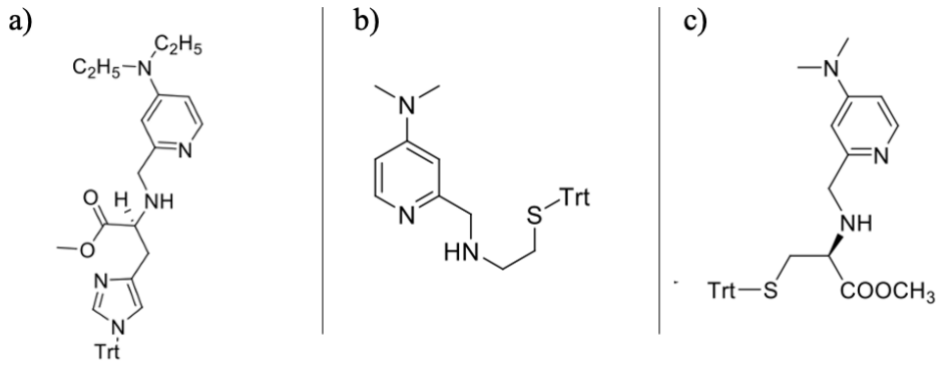

,

Figure 1.3: Chemical structures of SIRT2 inhibitors.

a) TH3, **b)** STC4, and **c)** SYTC1.

TH-3, a tritylhistidine derivative synthesized by Dr. Halil İbrahim Çiftçi's group, exhibited the most potent in vitro SIRT2 inhibition (IC50 = 1.3 μM) and significantly reduced the viability of MCF7 breast cancer cells (IC50 = 0.71 μM). Molecular docking studies confirmed the selective binding of TH-3 within the SIRT2 active site, suggesting a mechanism involving both SIRT2 inhibition and additional cellular effects (Ali et al., 2019). Similarly, STCY1 and STH4, also synthesized by Dr. Çiftçi's team, showed enhanced inhibitory potency relative to previous lead compounds, with STCY1 demonstrating specific interaction with the Ala135 residue of SIRT2 through its pyridine nitrogen, indicated by docking analyses (Radwan et al., 2020). These compounds exhibited strong antiproliferative effects against various cancer cell lines, highlighting their therapeutic potential. Co-crystallization experiments, which I am conducting in collaboration with the Structural Biology and Innovative Drug Development Center at Koç University (KUYBIIGM) under the supervision of Dr. Hasan Demirci, are currently underway to elucidate the detailed molecular interactions of these inhibitors with SIRT2. The high-resolution structures obtained from these studies will provide critical insights to guide rational drug design and optimization of more selective and potent SIRT2-targeted anti-cancer agents.

1.6 Structural Perspective on SIRT2

1.6.1 Structural Features of SIRT2

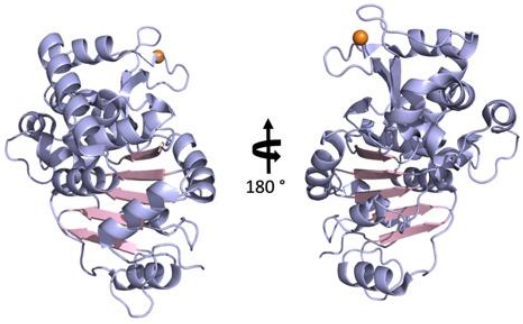

Figure 1.4: Illustration of apo-SIRT2 highlighting the Rossmann-like fold, shown with a 180-degree rotation around the y-axis.

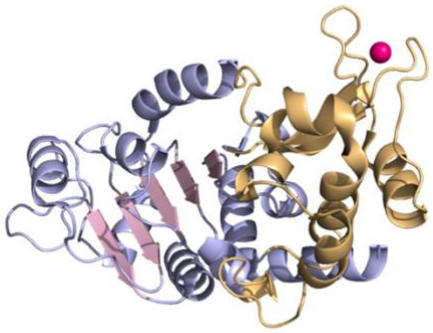

Figure 1.5: Illustration of SIRT2 domains: small domain (yellow), large domain (purple), Rossmann-like fold (pink), and Zn ion (magenta).

SIRT2 is characterized by a complex structural organization that plays a critical role in modulating its enzymatic activity and substrate specificity. Its structure comprises a well-defined catalytic core with an elongated shape, formed by two main domains: a larger Rossmann fold-like domain (residues 53–89, 146–186, and 241–356), which is typical of NAD(H)/NADP(H)-binding enzymes, and a smaller zinc-binding domain (residues 90–145 and 187–240) stabilized by a structural zinc atom (Finnin et al., 2001); Huang et al., 2017). These domains are connected by four polypeptide crossovers, creating a substantial groove at their interface, further shaped by three loops originating from the larger domain. The Rossmann fold contains six β-strands (β1–3 and β7–9)

arranged in a parallel β-sheet and is flanked by six α-helices (α1, α7, α8, and α10–α12) that provide structural stability and facilitate NAD binding through a conserved Gly-X-Gly motif (Finnin et al., 2001).

1.6.2 Role of Structural Biology in Drug Discovery

Structural biology is an important part of modern drug discovery. This technique provides detailed, three-dimensional structures of biological molecules which enables scientists to design small drugs that fit better and work more effectively (Liu et al., 2019). X-ray crystallography has proven to be very valuable, particularly in the early stages of drug development. Drugs such as Agenerase and Viracept (used for HIV), Relenza (for influenza), and cancer treatments like Gleevec and Tarceva demonstrate the usefulness of this method (Wlodawer & Vondrasek, 2017). Having detailed structures of proteins bound to their drug partners helps researchers improve drug-target interactions and reduce unwanted side effects.

Structural biology has evolved from focusing on individual proteins to employing faster, large-scale methods that support drug discovery on a broader scale. Initiatives like structural genomics increased accessibility to protein structures and promoted data sharing among researchers (Arrowsmith, 2024). These efforts accelerate the identification and validation of new drug targets and aid in developing chemical tools to better understand protein functions. Emerging technologies like cryo-EM and AI tools such as AlphaFold2 enable more accurate modeling of complex biological systems (Jumper et al., 2021). Integrating structural, computational, and chemical biology with open collaboration is expected to make drug discovery faster, more precise, and more accessible.

1.6.3 X-ray Crystallography

X-ray crystallography is a widely used technique for studying and understanding the structural dynamics of biomacromolecules. Successful protein crystallography requires a reliable source of protein along with effective purification and concentration protocols that yield homogeneous and soluble samples. The growth of protein crystals suitable for structure determination is often the most challenging and least well-

understood step in the process (Smyth and Martin, 2000). Crystallization involves carefully inducing a highly concentrated protein solution to precipitate as crystals. If this occurs too rapidly, precipitation happens instead of crystal formation. Several factors influence crystallization, including the choice and concentration of precipitant, buffer composition and pH, protein concentration, temperature, crystallization method, and the use of additives (Smyth and Martin, 2000; McPherson and Gavira, 2014). Common crystallization techniques include sitting-drop and hanging-drop vapor diffusion, microbatch under oil and batch method in vials (McPherson and Gavira, 2014).

Two years ago, our team installed Turkey's first single-crystal X-ray diffractometer, named Turkish DeLight. This home-source diffractometer enables high-resolution structure determination of biomacromolecules using single-crystal cryo-crystallography. The latest generation of home-source XRD instruments features intense and focused X-ray beams along with advanced optics, allowing rapid analysis of crystalline materials. The main hardware components include an X-ray generator, a sample holder, and an X-ray detector. Monochromatic X-rays are directed onto the crystal, producing diffraction patterns captured by the detector and processed via user-friendly software (Atalay et al., 2023). At Turkish DeLight, data collection can be performed at either cryogenic or ambient temperatures. Ambient temperature data are acquired by placing Terasaki crystallization plates directly into the XrystalCheck sample holder, a method our team was the first to publish globally. For cryogenic data collection, crystals are harvested from Terasaki plates using MiTeGen or microLoops sample pins according to crystal size, then rapidly frozen by plunging into liquid nitrogen. The frozen crystals are transferred to a pre-cooled sample puck, which is then mounted on the XRD sample holder. During data processing, strategy parameters such as detector distance and the selection of optimal diffraction frames are adjusted to guide efficient data collection.

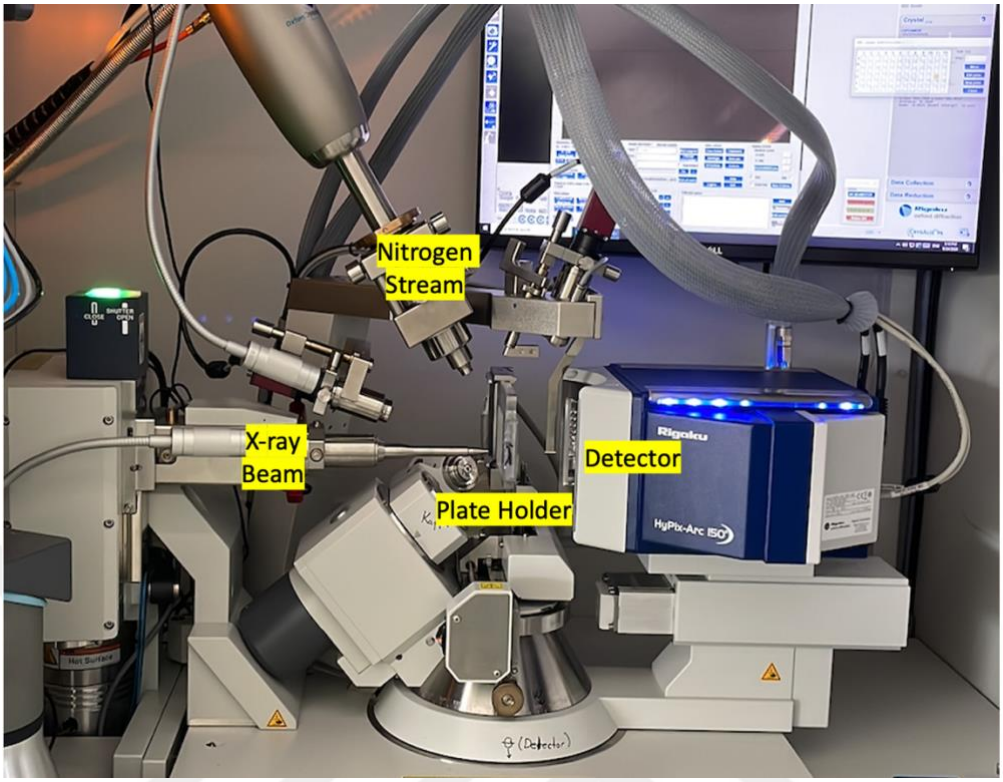

Figure 1.6: Illustration of out homesource X-ray diffractometer, Turkish DeLight

1.6.4 Aim of the Thesis

The available SIRT2 structures in the Protein Data Bank have predominantly been determined using cryogenic data collection techniques. While cryo-cooling increases crystal stability and data quality, it may mask the intrinsic flexibility and dynamic conformational states of the protein under physiological conditions. Investigating the protein structure at ambient temperature provides an opportunity to capture these native dynamics, particularly in regions critical for function such as the active site. The primary objective of this thesis is to determine the apo structure of SIRT2 at ambient temperature using X-ray crystallography. Subsequently, this structure will be compared with previously reported apo and inhibitor-bound SIRT2 structures to identify conformational differences, especially within the NAD^+ binding pocket and catalytic core. This comparative analysis aims to deepen our understanding of SIRT2's functional mechanisms and facilitate the design of more effective inhibitors.

Chapter 2:

MATERIALS AND METHODS

2.1 Bacterial Transformation

2.1.1 Plasmid Construction

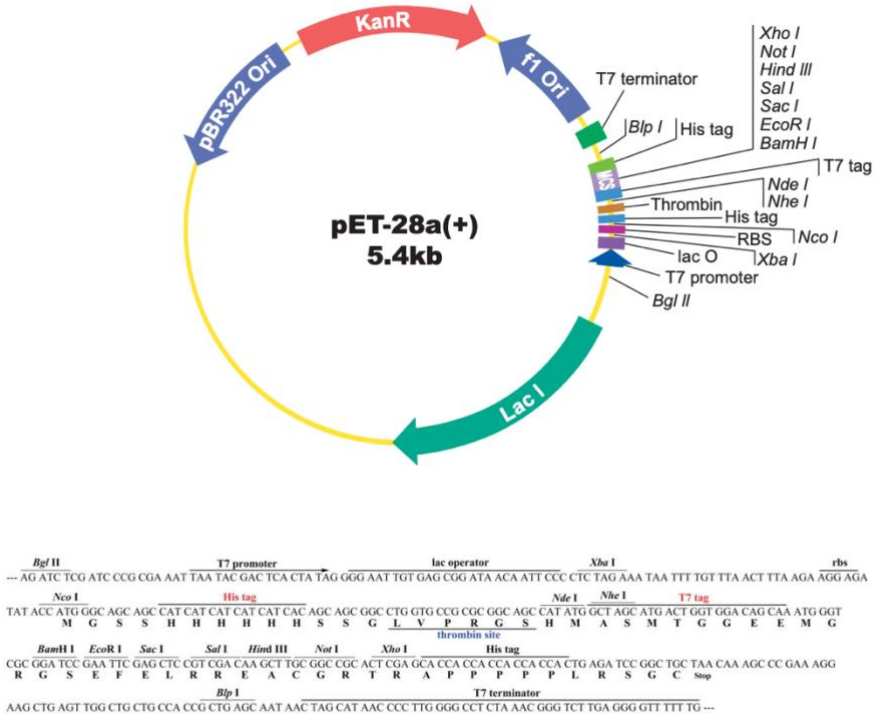

Figure 2.1: The schematic representation of the bacterial expression vector pET-23a(+) (GenScript)

SIRT2-SUMO:

MSDSEVNQEAKPEVKPEVKPETHINLKVSDGSSEIFFKIKKTTPLRRLMEAF
AKRQGKEMDSLRFLYDGIRIQADQTPEDLDMEDNDIIEAHREQIGGGHMER
LLDELTLEGVARYMQSERCRRVICLVGAGISTSAGIPDFRSPSTGLYDNLEK
YHLPYPEAIFEISYFKKHPEPFFALAKELYPGQFKPTICHYFMRLLKDKGLLL
RCYTQNIDTLERIAGLEQEDLVEAHGTFYTSHCVSASCRHEYPLSWMKEKI
FSEVTPKCEDCQSLVKPDIVFFGESLPARFFSCMQSDFLKVDLLLVMGTSLQ
VQPFASLISKAPLSTPRLLINKEKAGQSDPFLGMIMGLGGGMDFDSKKAYR
DVAWLGECDQGCLALAELLGWKKELEDLVRREHASIDAQS*

The SIRT2-SUMO fusion protein was expressed using the bacterial pET28a vector system, a commonly used vector for producing recombinant proteins in Escherichia coli. In this system, the target gene is placed under the control of a strong T7 promoter with a lac operator to help suppress uninduced, leaky expression. Protein synthesis is initiated via a Shine–Dalgarno (SD) sequence, which is derived from the gene 10 protein of the T7 bacteriophage and ensures efficient translation initiation (Shilling et al., 2020). In typical constructs, the gene of interest is cloned with a N-terminal 6xHis-tag and a thrombin protease cleavage site (TPS), allowing for affinity purification using standardized protocols. The pET28a vector also includes a T7 tag sequence, with an optional C-terminal His-tag, offering flexibility for purification strategies (Shilling et al., 2020). The plasmid encoding the SIRT2-SUMO fusion is approximately 6542 base pairs in length (PDB: 4RMG), and includes a kanamycin resistance gene, a multiple cloning site (MCS), and LacI repressor elements (Figure 2.1). The LacI protein regulates transcription by binding to the lac operator, while the MCS provides adaptability through a variety of restriction sites, including XhoI, NotI, EagI, HindIII, SalI, SacI, EcoRI, BamHI, NheI, NdeI, and NcoI. IPTG is used to induce protein expression by inactivating the LacI repressor that allows transcription initiation. To increase its solubility and stability in the soluble fraction, the SIRT2 protein was engineered as a fusion construct with a 12 kDa SUMO tag and estimated molecular weight of the SIRT2-SUMO fusion protein is approximately 45 kDa. Protein expression was successfully carried out in the C43(DE3) strain, which is specifically engineered to tolerate and express potentially toxic

proteins, making it well-suited for producing the SIRT2-SUMO fusion construct (Rosano & Ceccarelli, 2014).

2.1.2 Transformation

In the transformation process, 50 µL of C43Ccompetent cells and plasmids were thawed on ice. Then, 2 µL of plasmid DNA was added to the 50 µL of competent C43 cells in an Eppendorf tube, and the mixture was kept on ice for an additional 20 minutes. Another 50 µL aliquot of Rosetta™2 cells was kept aside as a control. Both tubes were subjected to a heat shock at 42°C for 45 seconds which is followed by incubation on ice for 2 minutes. Afterwards, 500 µL of Luria Broth (LB) medium (10 g/L NaCl, 10 g/L tryptone, and 5 g/L yeast extract) without any antibiotics was added separately to the control and transformed cells at room temperature to provide growing media. The cultures were incubated at 37°C for 90 minutes to allow growth, then plated on agar containing 50 µg/mL kanamycin (Cat#KB0286, Bio Basic, Canada) and grown overnight at 37°C. Single colonies were selected and cultured overnight in liquid LB medium supplemented with the appropriate antibiotics. To preserve the cultures, they were mixed 1:1 (v/v) with glycerol (750 µL culture + 750 µL glycerol) and stored in cryotubes at –80°C.

2.2 Protein Expression in Escherichia coli

2.2.1 Small-Scale Expression Trial

For small-scale expression of the SIRT2-SUMO fusion protein, an optimized protocol optimized for toxic protein production was followed. The growth medium used was Luria Broth (LB), composed of 10 g/L NaCl, 10 g/L tryptone, and 5 g/L yeast extract. As described in the transformation section, a specialized E. coli strain, C43(DE3), known for its tolerance to toxic protein expression was used. For induction, the cultures were grown to an OD600 of approximately 3.5, and expression was induced using 0.1 mM IPTG, one-quarter the concentration typically used in standard protocols. Protein expression was carried out at 18 °C for approximately 32 hours (1.5 days). Following harvesting process by centrifugation at 3500 rpm which separates pellets from the growth medium, cells were lysed by sonication in the lysis buffer. The lysate was clarified by

centrifugation at 10,000 rpm to separate the soluble and insoluble fractions, supernanant and pellet respectively. The resulting supernatant was incubated with 100 µL of Ni-NTA resin at 4 °C overnight for affinity purification. After washing with HisA buffer (200 mM NaCl, 20 mM Tris-HCl, 20 mM imidazole, pH: 8.5), the bound protein was eluted using HisB buffer (200 mM NaCl, 20 mM Tris-HCl, 250 mM imidazole, pH: 8.5). Eluted samples were subsequently analyzed by SDS-PAGE.

2.2.2 Large-Scale Expression Trial

For large-scale protein production, the cultures were initially grown overnight in 150 mL of LB medium. As the C43 strain does not contain inherent antibiotic resistance, only kanamycin was used to avoid any contamination. IPTG and antibiotics were added at a standard 1:1000 (v/v) ratio. Subsequently, 6 liters of LB medium (prepared at 50 g/L) were divided into four flasks, each containing 1.5 L, and inoculated with the overnight starter culture. These cultures were further incubated overnight until an OD600 of approximately 3.5 was reached. As described in Section 2.2.1, protein expression was induced with 0.1 mM IPTG (GoldBio, Cat#I2481C) at high cell density, and the cultures were incubated at 18 °C for 32 hours. Following expression, cells were collected by centrifugation and transferred into falcon tubes. The resulting cell pellets were stored at –45 °C until further use.

2.3 Large-Scale Purification Trial

2.3.1 Buffer solutions

The buffers used in these experimentations are shown as tables in Table 2.1, Table 2.2, and Table 2.3.

Reagent	*Final Concentration*	*Amount*
NaCl	200 mM	11.688 g
Imidazole	20 mM	1.362 g
Tris	20 mM	6.06 g
ddH_2O		Up to 1L
Total		1 L

Table 2.1: HisA Buffer

Reagent	*Final Concentration*	*Amount*
NaCl	200 mM	11.688 g
Imidazole	250 mM	117.019 g
Tris	20 mM	6.06 g
ddH_2O		Up to 1L
Total		1 L

Table 2.2: HisB Buffer

Reagent	*Final Concentration*	*Amount*
NaCl	500 mM	29.22 g
Imidazole	20 mM	1.362 g
Tris	50 mM	6.06 g
Glycerol	5% (v/v)	50 ml
Triton X-100	0.5%(v/v)	5 ml
ddH_2O		Up to 1L
Total		1 L

Table 2.3: Lysis Buffer

2.3.2 Affinity Chromatography

Cell pellets were resuspended in lysis buffer (500 mM NaCl, 20 mM imidazole, 50 mM Tris-HCl pH 8.5, 5% glycerol, 0.1% Triton X-100) and lysed via sonication. The lysate was separated to supernanant and pellet by ultracentrifugation at 35,000 rpm for 75 minutes. The cleared supernatant was filtered and loaded onto Ni-NTA affinity column using an AKTA Go system. The His-tagged fusion protein selectively bound the resin that allows contaminants to be washed away with HisA buffer. The protein was eluted using HisB buffer containing 250 mM imidazole. Eluates were concentrated using a 30 kDa Amicon ultrafiltration device (Merck Millipore). Freeze-thaw assays indicated that glycerol addition was unnecessary for protein stability. Aliquots were stored at –80°C, and the results were evaluated using SDS-PAGE **(Figures 3.2 , 3.4, and 3.5a)**.

2.3.3 SUMO Tag Cleavage and Reverse Affinity Chromatography

Cleavage of the SUMO-tag was optimized by incubating SIRT2-SUMO with ULP1 protease at varying enzyme-to-substrate ratios (1:1000, 1:50, 1:10 v/v) overnight at 4°C. The most efficient cleavage was observed with a 1:1000 ratio **(Figure 3.3)**. Following cleavage, reverse affinity chromatography was performed using Ni-NTA resin to remove the cleaved SUMO and His-tags. The cleaved, tag-free Sirt2 protein did not bind the resin and was collected in the flow-through, while SUMO and His-tag fragments were hold **(Figure 3.4 and Figure 3.5b)**. The purified protein was concentrated for the crystallization trials.

2.4 Crystallization of SIRT2

SIRT2 crystallization trials were conducted using the microbatch method, in which equal volumes of protein and precipitant solutions were mixed in Terasaki plate wells and overlaid with paraffin oil to prevent evaporation (Atalay et al., 2023). Typically, 0.83 µL of protein was combined with 0.83 µL of crystallization solution. A range of protein concentrations and incubation conditions at both room temperature and 4 °C were tested to improve crystal quality and an extensive screen of over 3000 different

crystallization conditions was used. Drop ratios were optimized to enhance the size, morphology, and stability of the crystals. Despite these efforts, only poorly diffracting crystals were initially obtained. To improve crystal quality, several optimization strategies inspired by previous crystallization studies were applied. One particularly effective condition which is originally reported for the apo-SIRT2 structure (PDB ID: 8XE7) consisting of 23% (w/v) PEG 3350 and 0.1 M Bis-Tris at pH 6.0 was tested using 1:1, 1:2, 1:3, 2:1, 1.5 protein-to-reservoir ratios. Finally, well-ordered SIRT2 crystals were successfully obtained in a reproducible manner using 1:2 and 1:3 protein-to-reservoir ratios **(Figure 3.6)**.

2.5 X-ray Data Collection and Processing

Diffraction data were collected using the home-source X-ray diffractometer "Turkish DeLight" at ambient temperature (298 K). Eleven apo-SIRT2 crystals were used, and a total of 11 datasets were collected. During collection, the detector was positioned 130 mm from the sample, and X-ray beam intensities of 10% and 20% were applied. Data were collected across an omega range of –21.2° to 26.7°, using a fine-slicing step size of 0.2°. Each crystal was exposed for 10, 20, and 30 seconds until it became damaged and stopped diffracting. The collected datasets were processed using CrysAlisPro (Rigaku Oxford Diffraction). Multiple datasets were loaded together, allowing for simultaneous peak finding and unit cell determination to ensure consistency. Data merging was carried out using the 'xx proffitbatch' command, followed by a reduction step with a custom script. The final merged dataset was produced using the ProffitMerge function and saved as an .mtz file after finalization for downstream structure determination **(Table 3.1)**.

2.6 Structure Determination and Refinement

Structure determination of SIRT2 was carried out using the PHENIX software suite. The amino acid sequence of SIRT2 was prepared in FASTA format (PDB ID: 4RMG), and molecular replacement was performed using the apo-human SIRT2 structure (PDB ID: 8XE7) as the search model. Multiple models were explored to optimize the

replacement process, 8XE7 was the most suitable template. Afterwards, initial rounds of refinement were conducted with phenix.refine which focuses on optimizing R-work and R-free values to reduce overfitting. Manual model building and validation were performed in COOT which allows visual inspection and corrections based on the electron density maps. The final structure of SIRT2 was refined at 2.80 Å resolution using data collected from our in-house X-ray diffractometer, Turkish DeLight. The crystals belonged to the monoclinic space group P 1 21 1, with unit cell parameters of 36.66 × 75.04 × 55.62 Å and angles of 90.0°, 95.4°, and 90.0°. The refinement statistics indicate an R-work of 23.05% and an R-free of 31.29%. The final model includes 2,135 atoms, consisting of 282 protein residues and one zinc ion; no water molecules were modeled. Geometry validation shows a well-refined structure, with root-mean-square deviations of 0.011 Å for bond lengths and 1.14° for bond angles. According to the Ramachandran plot, 93.88% of residues are in favored regions with no outliers in disallowed regions. The overall dataset completeness is 92.85%, while the highest resolution shell exhibits 62.42% completeness **(Table 3.2)**.

Chapter 3:

RESULTS

3.1 Protein Expression and Purification Outcomes

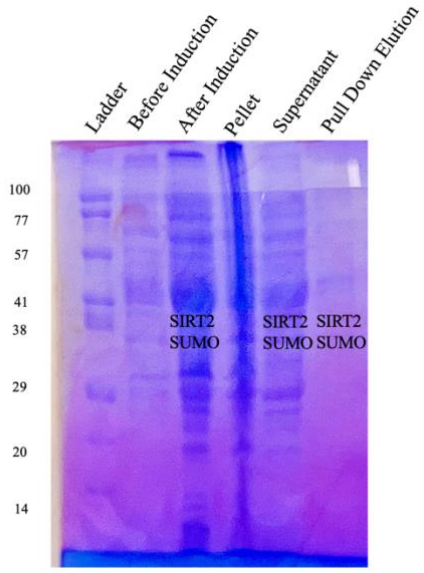

Figure 3.1: SIRT2-SUMO Small Scale Protein Expression SDS-gel Results

Figure 3.1 presents the initial protein expression results of the SIRT2-SUMO fusion construct. The SDS-PAGE gel displays samples collected in the following order: before-induction, after-induction, pellet, supernatant, and pull-down elution. The expected molecular weight of the SIRT2-SUMO fusion protein is approximately 45 kDa. A faint band observed in the pre-induction lane suggests that there is minimal leaky expression. In contrast, distinct bands around 45 kDa in the after-induction and supernatant lanes confirm the successful overexpression of the target protein. Moreover, the presence of a clear band in the pull-down elution sample indicates that the His-tag is accessible and the fusion protein was successfully purified. As detailed in Section 2.2.2, SIRT2-SUMO expression was achieved under optimized conditions, including induction at a high cell density ($OD_{600} \approx 3.5$) with 0.1 mM IPTG and prolonged incubation. This gel represents the final step of the small-scale expression optimization process.

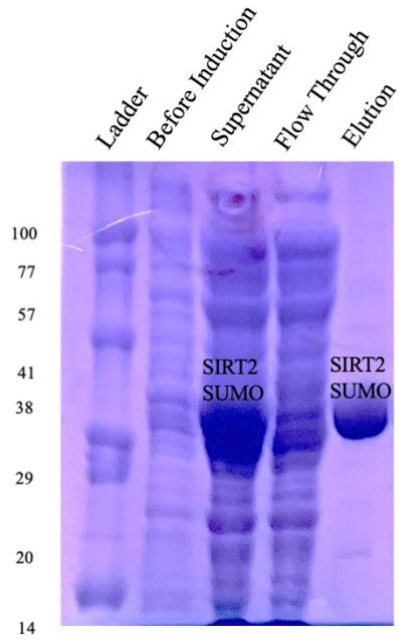

Figure 3.2: SIRT2-SUMO Large-Scale Protein Expression SDS-gel Results

Figure 3.2 presents the results of the initial large expression of the SIRT2-SUMO fusion protein. For this experiment, 1 L of rich LB medium was used and protein expression was performed as described in Section 2.2.2. Purification was performed using affinity chromatography on an ÄKTA go system. The SDS-PAGE gel illustrates before induction, supernatant, flow-through, and elution respectively. Compared to small-scale trials, leaky expression was largely eliminated in this setup. Furthermore, protein yield increased substantially, and the elution fraction shows a clear band at the expected molecular weight (~45 kDa), indicating successful purification of the SIRT2-SUMO protein in a pure form.

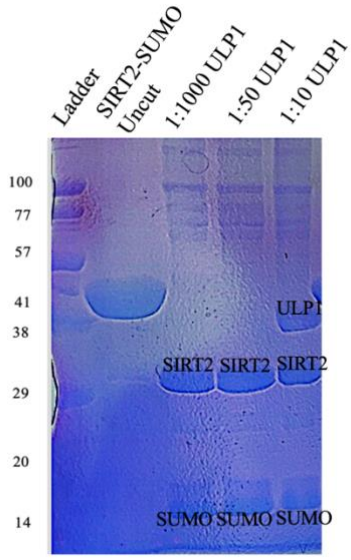

Figure 3.3: SIRT2-SUMO – ULP1 Cleavage Test Results

Figure 3.3 illustrates the results of SUMO-tag cleavage trials from the SIRT2-SUMO fusion protein using ULP1 protease. Both overnight and 4-hour cleavage reactions were performed at 4 °C, using varying volume ratios of ULP1 to SIRT2-SUMO (v/v). The SDS-PAGE gel shows, in order: uncut SIRT2-SUMO, and samples with ULP1 added at 1:1000, 1:50, and 1:10 (v/v) ratios. Only the 4-hour cleavage results are presented in this figure. As shown in lane 3, the SUMO-tag was effectively cleaved using a 1:1000 ULP1:SIRT2-SUMO ratio, even within a short incubation period and at low protease concentrations. These results demonstrate that the ULP1 enzyme efficiently cleaves the fusion construct.

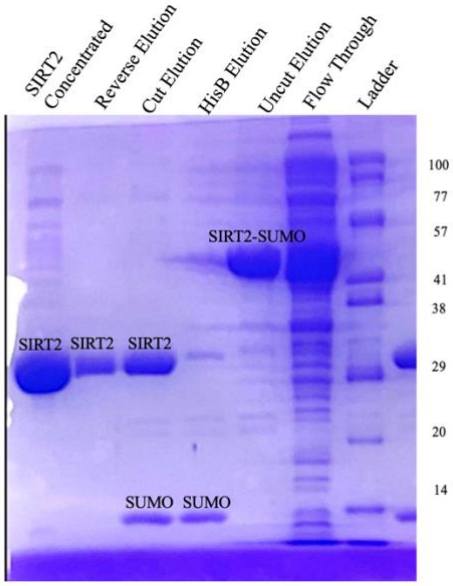

Figure 3.4: SIRT2-SUMO – ULP1 Cleavage and Reverse Chromatography SDS-gel results

Figure 3.4 illustrates the successful cleavage of the SUMO tag from the SIRT2-SUMO fusion protein using ULP1 at a 1:1000 (v/v) ratio, followed by purification of the cleaved SIRT2 protein. The SDS-PAGE gel shows, in order: concentrated SIRT2, reverse affinity chromatography elution (cleaved SIRT2), cut SIRT2 sample, His-binding elution (containing SUMO tag and ULP1—while the SUMO tag is clearly visible, ULP1 is present only in trace amounts and is not detectable), uncut SIRT2-SUMO, and supernatant. This gel confirms that the SUMO tag was efficiently cleaved without any detectable degradation of the target protein and that cleaved SIRT2 was successfully separated from the tag and protease via reverse His-tag affinity chromatography. The final concentration of the purified SIRT2 protein was performed using a 30 kDa concentrator. The resulting concentrated protein was subsequently used in crystallization trials.

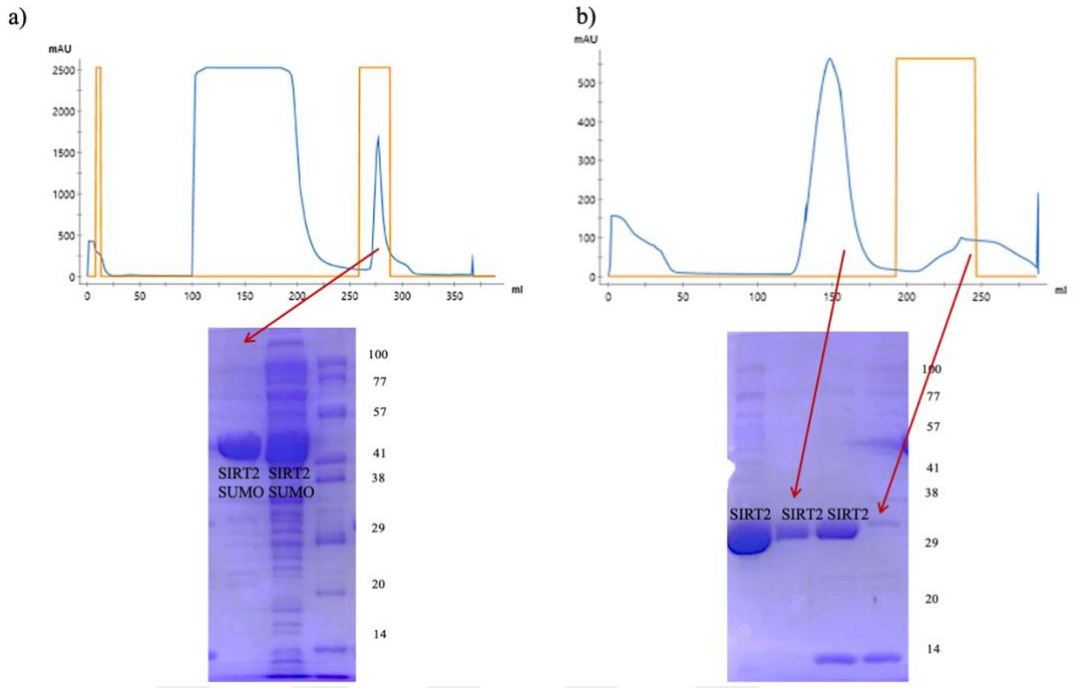

Figure 3.5: Detailed Analysis of Affinity and Reverse Chromatography of SIRT2, Including Chromatograms and SDS-PAGE Results

Figure 3.5 illustrates the large-scale purification process of the SIRT2-SUMO fusion protein, followed by SUMO-tag cleavage and reverse chromatography to obtain purified SIRT2 suitable for crystallization trials. Figure 3.6(A) displays the chromatogram from the Ni-NTA affinity chromatography. Following the application of 225 mL of clarified supernatant containing SIRT2-SUMO, approximately 80 mL of the fusion protein was successfully eluted, as confirmed by a prominent band around 45 kDa in the SDS-PAGE gel (lane 1). Figure 3.6(B) shows the chromatogram from the reverse His-tag chromatography, performed after ULP1-mediated SUMO cleavage. This step enabled separation of the cleaved SIRT2 (non-His-tagged) from the His-tagged SUMO and ULP1. Approximately 50 mL of pure SIRT2 protein was recovered, as evidenced by the SDS-PAGE gel. The resulting purified SIRT2 protein was subsequently concentrated using a 30 kDa centrifugal filter unit and used for downstream crystallization experiments.

3.2 Crystallization Conditions and Crystal Morphology

To obtain diffracting-quality SIRT2 crystals, extensive crystallization trials were conducted using a range of protein concentrations and incubation conditions, including both room temperature and 4 °C. Despite numerous attempts, only poorly diffracting crystals were initially obtained. To improve crystal quality, various optimization strategies based on literature precedents were explored. Among these, the crystallization condition reported for the apo-SIRT2 structure (PDB ID: 8XE7) containing 23% (w/v) PEG 3350 and 0.1 M Bis-Tris buffer at pH 6.0 successfully produced SIRT2 crystals. When crystallization was replicated with this condition, crystals were successfully reproduced **(Figure 3.6)**.

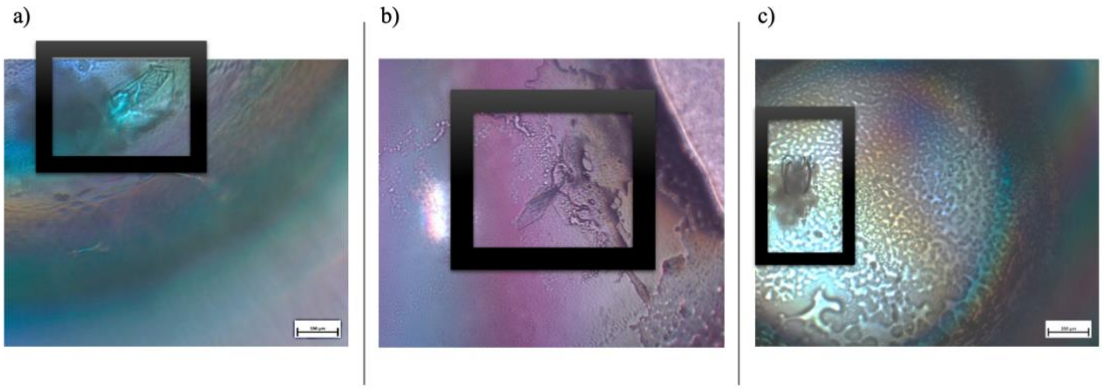

Figure 3.6: Polarized Light Microscopy Images of Apo-SIRT2 Crystals

Figure 3.6 illustrates polarized light microscopy images of APO-SIRT2 crystals obtained using a crystallization solution containing 23% (w/v) PEG 3350 and 0.1 M Bis-Tris buffer at pH 6.0. Panels (a), (b), and (c) illustrate APO-SIRT2 crystals with their morphology and birefringence characteristics.

3.3 X-ray Diffraction and Data Processing

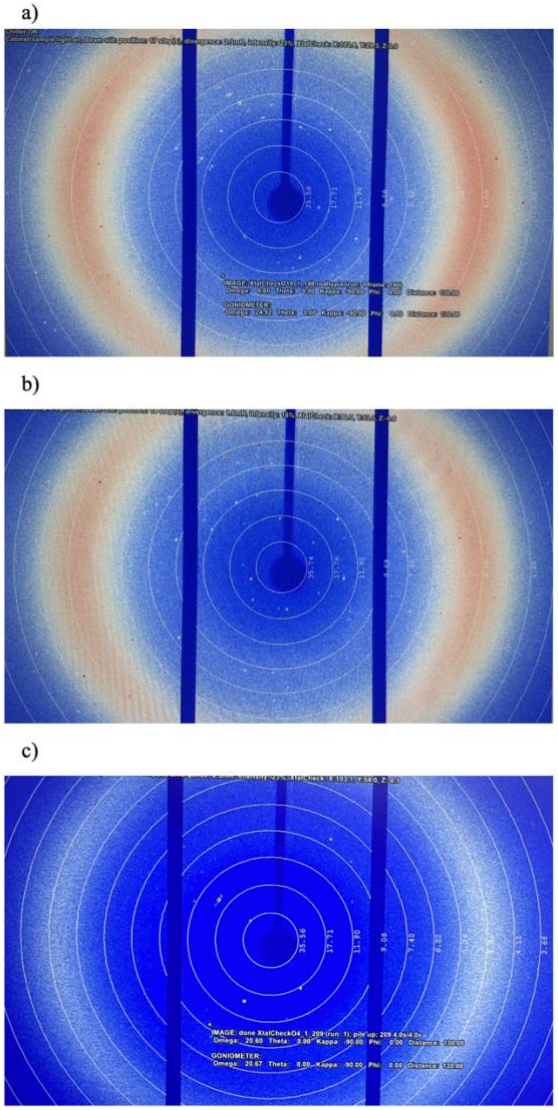

Figure 3.7: Diffraction Results of SIRT2 Crystals

Panels (a), (b), and (c) present diffraction images of SIRT2 crystals collected at 298 K using our home X-ray diffraction system, Turkish DeLight. Data collection was performed at 10% and 20% X-ray beam intensities, with a fixed detector distance of 130 mm. Exposure times were sequentially increased to 5, 10, 20, and 30 seconds per frame until the crystal exhibited signs of radiation damage. Diffraction data were successfully obtained to a resolution of 3.0 Å. A total of eleven datasets were collected during the experiment.

resolution (A)	# kept	#theory	#unique	% complete	average redundancy	mean F2	mean F2/sig(F2	Rint	SigmaB	CC ½	CC*	deltacc	Rurim	Rpim
30.99- 5.20	16939	1190	1182	99.3	14.3	47.80	8.98	0.383	0.120	0.944	0.986	0.0506	0.403	0.099
5.20- 4.11	17229	1190	1190	100.0	14.5	46.90	7.13	0.431	0.153	0.922	0.980	0.0490	0.461	0.112
4.11- 3.58	15556	1190	1189	99.9	13.1	27.16	5.36	0.496	0.239	0.880	0.968	0.0460	0.545	0.135
3.58- 3.25	12642	1190	1190	100.0	10.6	14.50	3.54	0.573	0.465	0.617	0.874	0.0272	0.803	0.182
3.25- 3.01	7051	1190	1143	96.1	6.2	8.94	2.32	0.730	0.820	0.128	0.477	-0.0077	2.133	0.353
3.01- 2.84	3248	1190	1018	85.5	3.2	5.51	1.02	0.918	1.099	0.069	0.360	-0.0119	7.223	0.620
2.84- 2.69	1777	1190	852	71.6	2.1	1.66	0.38	0.956	1.259	0.017	0.183	-0.0157	47.231	0.756

Table 3.1: Data Reduction Statistics from CrysAlisPro

This table summarizes the output parameters obtained from data reduction of SIRT2 crystal diffraction images using the CrysAlisPro software. Diffraction data were processed up to 2.7 Å resolution.

PDB ID	N/A
Data collection	SIRT2
R-work / R-free	0.2305 / 0.3129
X-ray source	Turkish DeLight
No. atoms Total:	2135
Protein residues	282
Ligand	(Zn):1
Water molecules	0
Temperature (K) : 298	298
Space Group	P 1 21 1
Unit cell parameters	36.66 75.04 55.62 90.0 95.40 90.0
Resolution	30.994 - 2.80 Å
Completeness (%)	92.85% overall (62.42% in highest shell)
Bond lengths (Å)	RMSD: 0.011
Bond angles (°)	RMSD: 1.14
Refinement Resolution	2.80 Å
No. reflections	6871
Ramachandran favored (%)	93.88%
Ramachandran allowed (%)	6.12%
Ramachandran disallowed (%)	0.00%

Table 3.2: Refinement Statistics from Phenix

3.4 Structural Analysis of Apo-SIRT2 at Ambient Temperature and Its Comparison with Existing Structures

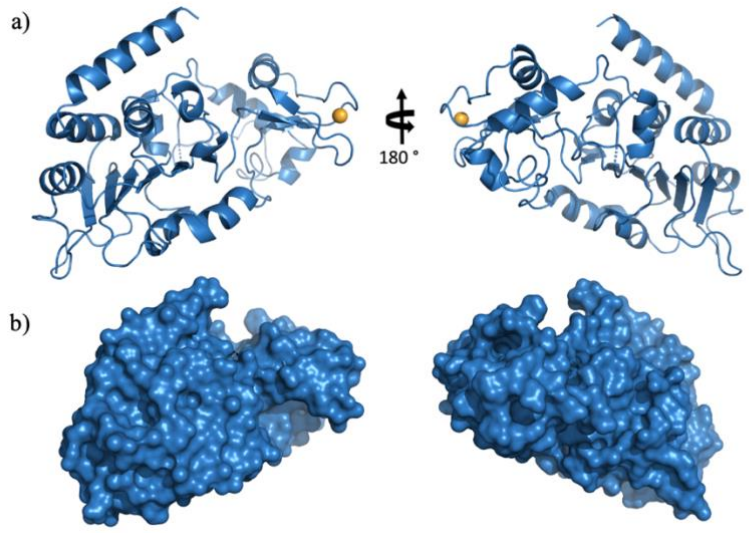

Figure 3.8: Apo structure of SIRT2 protein at ambient temperature

a) Cartoon representation of apo-SIRT2, shown from the front and rotated 180° around the y-axis. b) Surface representation of apo-SIRT2, shown from the front and rotated 180° around the y-axis.

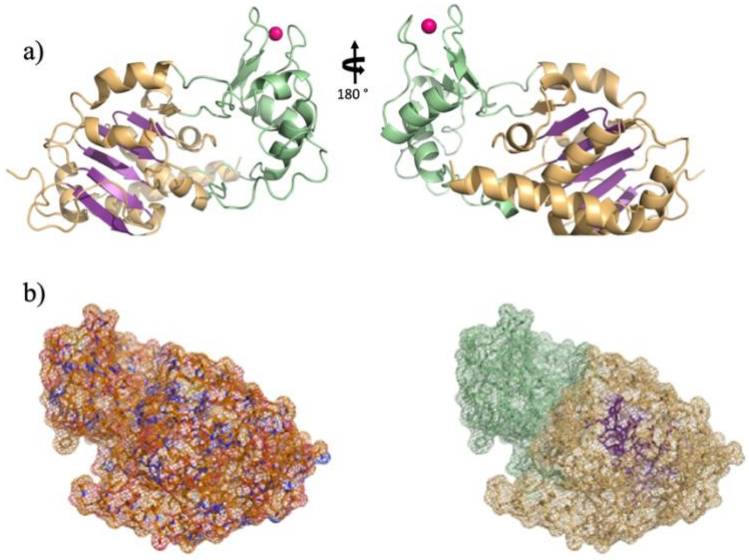

Figure 3.9: The domain organization of apo-SIRT2 showing the small domain, the large Rossmann-like fold domain, and the zinc-binding domain

The structure of apo-SIRT2 is shown with its distinct domains is shown: the large domain in yellow, the Rossmann-like fold domain in pink, and the small zinc-binding domain in green. The zinc ion is represented as a magenta sphere. a) Colored cartoon representation with the domains clearly distinguished. b) Left: overall meshed stick representation of apo-SIRT2. Right: domains separated by color: small domain in green and large domain in yellow.

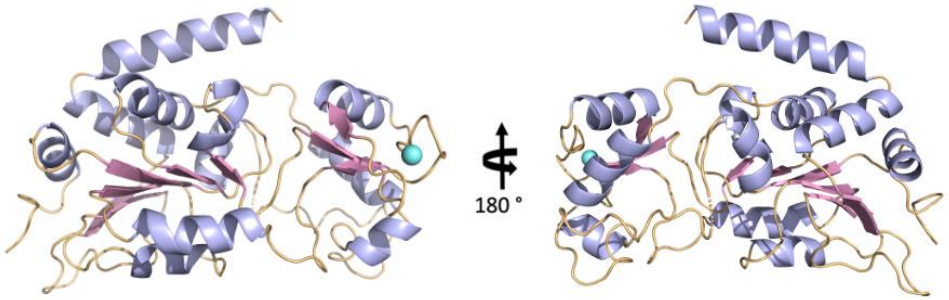

Figure 3.10: Secondary structure organization of apo-SIRT2

Cartoon representation of the secondary structure elements with a 180° rotation around the y-axis. α-helices are shown in purple, β-sheets in pink, and loops in wheat.

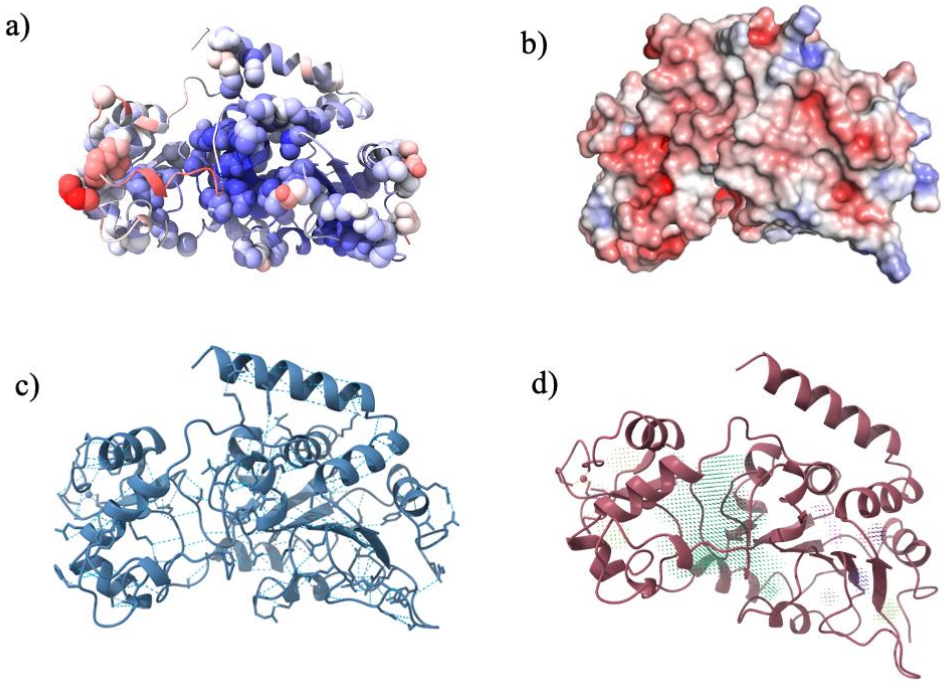

Figure 3.11: Structural features of apo-SIRT2 at ambient temperature

a) Surface representation of apo-SIRT2 colored by B-factor values: red indicates flexible regions, white moderate, and blue rigid regions. b) Electrostatic surface potential map of apo-SIRT2 showing the distribution of negative (red, −5000) to positive (blue, +5000) charges across the catalytic cleft and interdomain surfaces. c) Visualization of the internal hydrogen bond network showing interactions that stabilize the NAD^+ binding pocket and domain interfaces. d) Surface cavity analysis revealing accessible tunnels and pockets, potential ligand-binding sites within the structure.

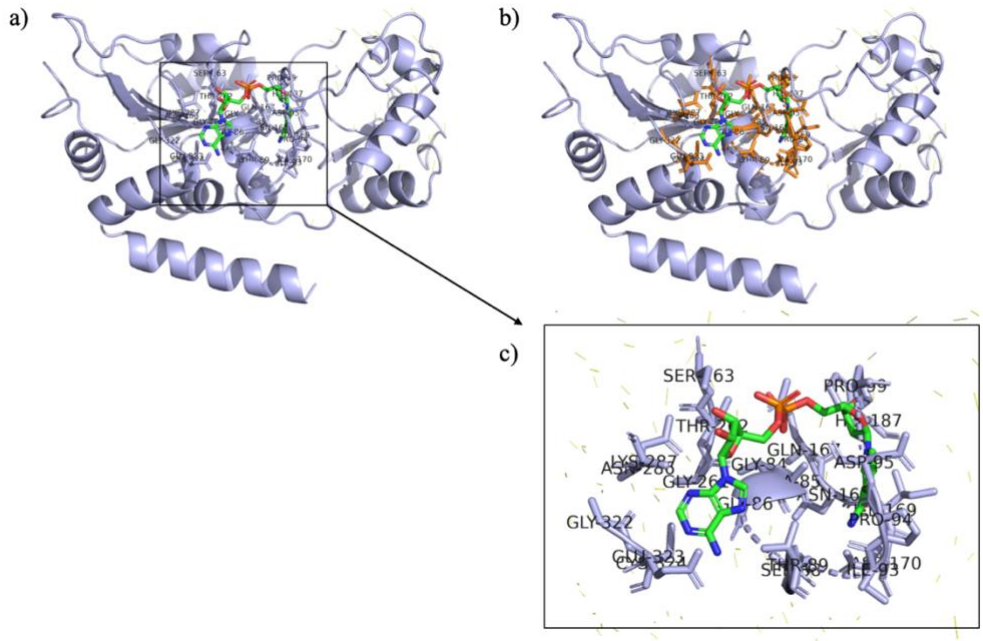

Figure 3.12: A detailed view of the NAD⁺ binding pocket in the apo-SIRT2 structure emphasizing how residues involved in binding are positioned in the absence of the cofactor

a) Superimposition of NAD^+ from the PDB: 4RMG structure onto the apo-SIRT2 structure, with interacting residues labeled. b) Interacting residues are shown in orange stick representation with residue labels. c) Close-up view of the NAD^+ molecule and its surrounding interacting residues.

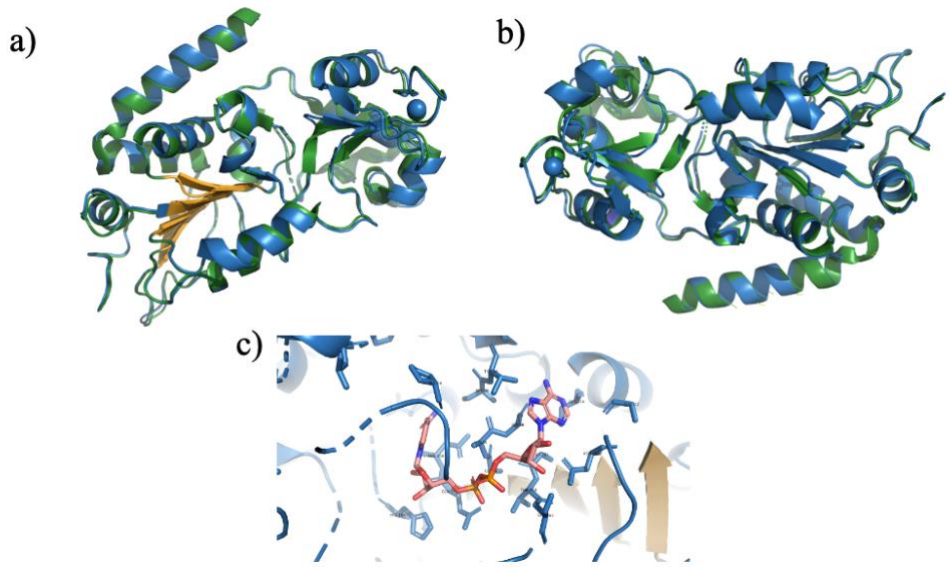

Figure 3.13: Structural comparison of ambient apo-SIRT2 with the apo-SIRT2 crystal structure (PDB ID: 8XE7).

a) Structural alignment of apo-SIRT2 (blue) and 8XE7 (green) using residues 79–83, 161–166, 256–260, 282–286, and 317–321 through Rossmann-like fold (orange) and showing subtle conformational differences. b) Alignment based on helix-forming residues 336–354 shows minor conformational changes between the two apo forms. c) Close-up view of the NAD^+ molecule superimposed onto the apo-SIRT2 structure with interacting residues displayed.

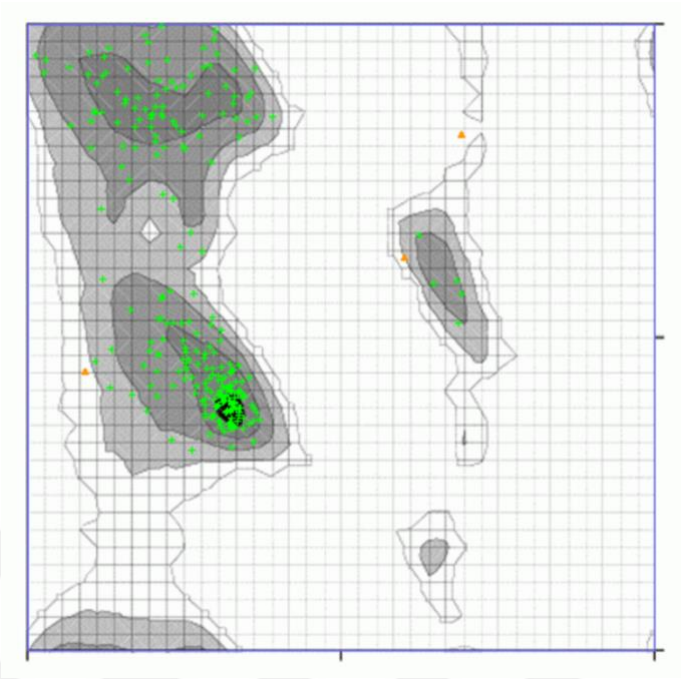

Figure 3.14: Ramachandran plot of ambient apo-SIRT2 showing backbone dihedral angle distribution.

The crystal structure of human SIRT2 was successfully refined at a resolution of 2.80 Å using X-ray diffraction data collected with a home-source diffractometer called Turkish DeLight. The crystals belonged to the monoclinic space group P 1 21 1, with unit cell dimensions of about 36.66 Å by 75.04 Å by 55.62 Å, and angles of 90°, 95.4°, and 90°. The final model includes 2,135 atoms, made up of 282 protein residues and one zinc ion, but no water molecules were modeled. Refinement statistics showed an R-work of 23.05% and an R-free of 31.29%, which are within an acceptable range for this level of resolution. The geometry of the structure was well validated, with very small deviations in bond lengths (0.011 Å) and bond angles (1.14°). According to the Ramachandran plot, nearly 94% of residues fall into favored regions, with no residues in disallowed regions, indicating good overall stereochemistry. The dataset was 92.85% complete overall, although completeness dropped to 62.42% in the highest resolution shell (**Table 3.2)**.

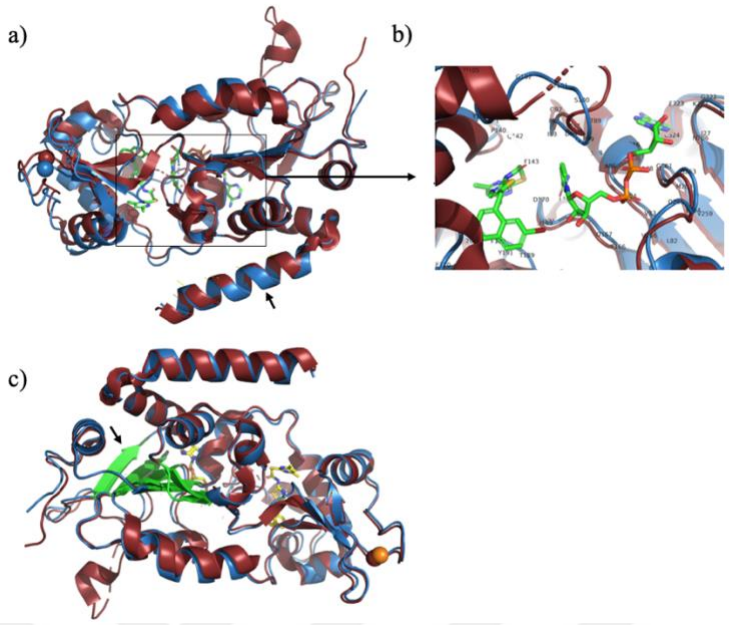

Figure 3.15: Comparison of apo-SIRT2 with the NAD⁺ and SirReal2-bound SIRT2 structure (PDB ID: 5DY4) reveals groove compaction and inhibitor-induced structural rearrangements.

a) Structural alignment of apo-SIRT2 (blue) and 5DY4 (red) based on helix-forming residues 336–354. b) Close-up view of the aligned structures showing the positions of NAD^+ and SirReal2 within the binding pocket. c) Structural alignment using residues 79–83, 161–166, 256–260, 282–286, and 317–321 showing conformational differences in the Rossmann-like fold (green).

Analyzing the flexibility of the structure through B-factor values revealed that the most flexible region lies between Pro99 and His111. This area includes a loop that extends outward from the protein core. On the other hand, some of the most rigid parts are within the Rossmann-like fold domain, specifically near Thr166 and Asp286. The smaller domain of the protein, which includes the zinc coordination site, showed average flexibility. This region also occupies the conserved inhibitor binding site formed by residues Phe96, Ile118, Ala135, Phe190, Ile232, and Val233. In contrast, the larger domain of the protein is much more rigid overall. Particularly, the NAD^+ binding site is located close to the Rossmann-like fold which corresponds to one of the more rigid regions (**Figure 3.10a)** .To understand conformational differences, the ambient-temperature structure was compared with several previously solved SIRT2 structures determined at cryogenic temperatures: 8XE7 (cryo-apo), 4RMG (complexed with NAD^+ and SirReal2 called 3TE), and 5YD4 (complexed with NAD^+ and a SirReal2 analog called 5GN).

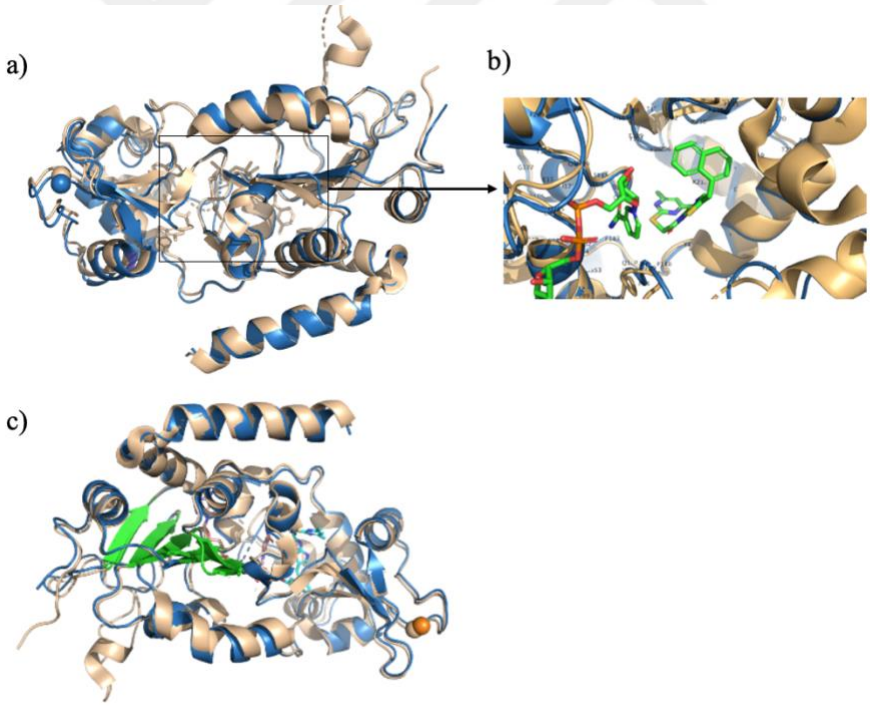

Figure 3.16: Comparison of apo-SIRT2 with the NAD^+ and SirReal2-bound SIRT2 structure (PDB ID: 4RMG) displays groove narrowing and conformational changes induced by inhibitor binding.

a) Structural alignment of apo-SIRT2 (colored in blue) and 4RMG (colored in wheat) based on helix-forming residues 336–354. b) Close-up view of the aligned structures showing the positions of NAD^+ and SirReal2 within the binding pocket. c) Structural alignment based on residues 79–83, 161–166, 256–260, 282–286, and 317–321 showing conformational differences in the Rossmann-like fold (colored in green).

RMSDs calculated showed a high degree of similarity with the ambient structure and 8XE7 aligned with an RMSD of 0.463 Å **(Figure 3.15).** The inhibitor-bound structures 4RMG and 5YD4 showed slightly larger deviations of 0.684 Å (**Figure 3.16)** and 0.769 Å (**Figure 3.17)**, respectively. A detailed examination of the NAD^+-interacting residues across these structures revealed several notable differences. In our ambient temperature apo structure, NAD^+ was superimposed and the residues located within 3.5 Å of the ligand were identified as Gly84, Ala85, Gly86, Ser88, Thr89, Pro94, Gln167, Asn168, His187, Gly261, Thr262, Ser263, Asn286, Gly322, and Cys324 (**Figure 3.12)**.These residues form the core NAD^+ binding pocket, which is highly conserved among class III histone deacetylases. No interactions were detected between SirReal2 and any residues in our structure within a 5 Å cutoff. This suggests that in the absence of ligand or cofactor, the binding groove may adopt a narrower and more closed shape. In contrast, the cryogenic co-crystal structure 4RMG displayed a wider and more extended network of interactions with NAD^+ and the SirReal2 analog 3TE **(Figure 3.16a and 3.16b)**. Besides the residues shared with our apo structure, this network includes Phe96, Ile118, Phe119, Ala135, Pro140, Phe190, Ile232, and Val233. The 5YD4 structure solved with NAD^+ and the SirReal2 analog 5GN showed a similar interaction pattern. It shares several residues with 4RMG such as Phe96, Ile118, Ala135, Phe190, Ile232, and Val233. In addition, it forms extra contacts with Phe131 and polar or charged residues including Asp95, Arg97, Ile169, Asp170, Lys287, Glu288, and Glu323 (**Figure 3.15a and 3.15b)**. Despite these differences, both 4RMG and 5YD4 consistently contain a core set of conserved residues which are Phe96, Ile118, Ala135, Phe190, Ile232, and Val233 that form the active site for SirReal2-like inhibitors.

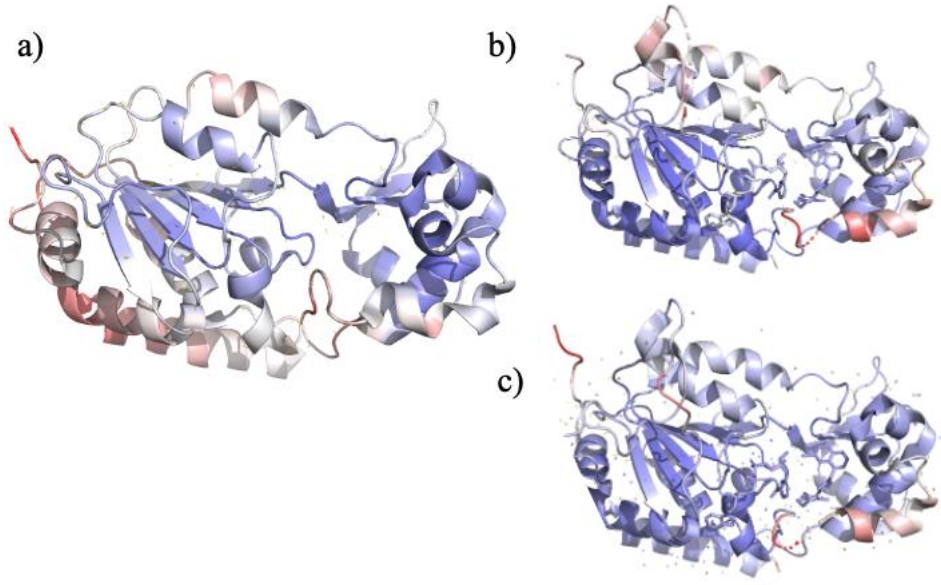

Figure 3.17: RMSD-based visualization of structural differences among 8XE7, 4RMG, and 5DY4 relative to apo-SIRT2.

RMSD mapping was applied to each structure to highlight regions of structural variability, where (a) shows 8XE7, (b) shows 4RMG, and (c) shows 5DY4. Color coding represents the degree of deviation: red indicates regions with high structural differences (high RMSD), white indicates moderate differences, and blue marks well-aligned regions with low RMSD values

Chapter 4:

DISCUSSION AND CONCLUSION

The ambient-temperature apo structure of human SIRT2 determined in this study provides insights into the protein's native conformational state that captures aspects of its behavior under near-physiological conditions. Structural biology techniques, particularly X-ray crystallography, have long relied on cryogenic data collection to improve crystal stability and reduce radiation damage during data acquisition. However, cryo-cooling can restrict the natural flexibility of proteins and sometimes induce conformations that differ from those found in physiological environments. By determining the structure at ambient temperature, this work offers a complementary perspective that reflects the true dynamic nature of SIRT2 as it exists in vivo. Understanding the precise structural details of SIRT2's active site and ligand-binding pockets is crucial for the rational design of inhibitors with therapeutic potential, particularly given the enzyme's implication in cancer, neurodegenerative diseases, and metabolic disorders.

The ambient-temperature apo structure presented here reveals that the overall fold of SIRT2 remains largely conserved compared to previously solved cryogenic structures. This finding aligns well with the expected structural stability of the Rossmann-fold and zinc-binding domains, which form the enzyme's core architecture **(Figures 18a, 15c, and 16c)**. Despite this global conservation, minor but functionally important local differences were observed, especially near the active site (**Figures 15c and 16c**). Structural alignments using DALI indicated low root mean square deviations (RMSDs) of 0.4 Å for the apo cryogenic structure (8XE7) and approximately 1.0 Å for inhibitor-bound structures 4RMG and 5YD4 (**Figure 4.1**). These values indicate that the presence of ligands induces conformational changes are significant enough to influence binding and enzymatic activity. This suggests a dynamic interplay between ligand binding and protein flexibility that modulates the shape and properties of the active site. A key observation from the ambient-temperature apo structure is the identification of residues forming the NAD^+ binding pocket, which are highly conserved among class III histone deacetylases.

These include Gly84, Ala85, Gly86, Ser88, Thr89, Pro94, Gln167, Asn168, His187, Gly261, Thr262, Ser263, Asn286, Gly322, and Cys324.

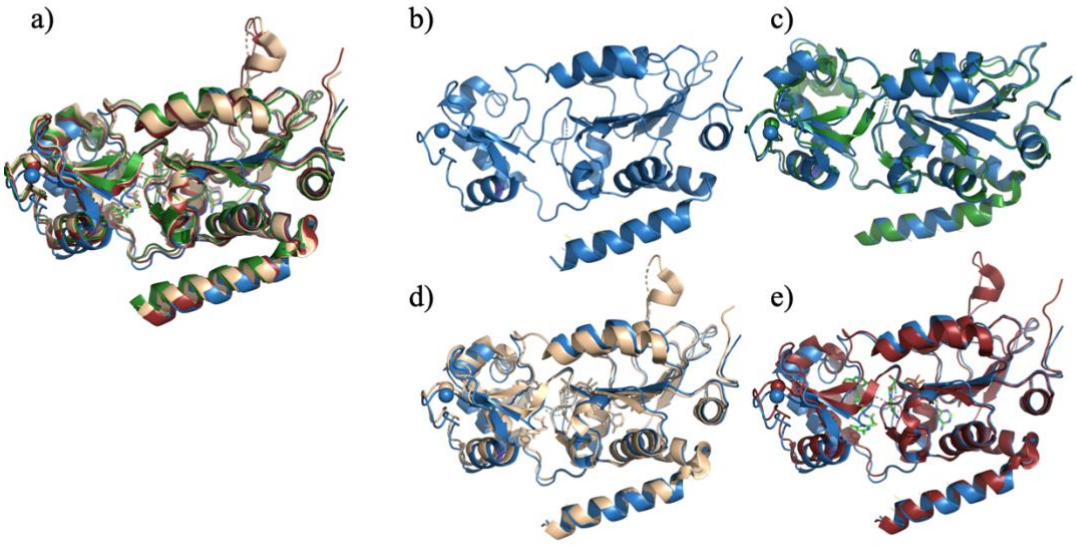

Figure 4.1: Combined structural superposition of apo-SIRT2 with 8XE7, 4RMG, and 5DY4 displays cumulative variability in the cofactor and ligand-binding regions.

a) Overall alignment of all structures. b) Ambient temperature apo-SIRT2 (blue). c) Superposition of apo-SIRT2 (blue) with 8XE7 (green). d) Superposition of apo-SIRT2 (blue) with 4RMG (wheat).e) Superposition of apo-SIRT2 (blue) with 5DY4 (red).

The consistency of these residues with known NAD^+ binding motifs supports the physiological relevance of this ambient structure. Particularly, no interactions were detected between the SirReal2 inhibitor and residues within 5 Å in this structure which indicate that in the absence of ligand or cofactor, the binding groove adopts a more closed conformation. This closed conformation probably represents the inactive or resting state of SIRT2 under conditions that closely mimic its natural environment that offers a more reliable reference point for observing structural changes triggered by ligand binding. In comparison, the cryogenic co-crystal structures 4RMG and 5YD4 (both solved in the presence of NAD^+ and SirReal2 analogs) demonstrate more extensive interaction networks within the binding pocket. The 4RMG structure features additional hydrophobic

residues such as Phe96, Ile118, Phe119, Ala135, Pro140, Phe190, Ile232, and Val233, which appear to create a more open and accommodating pocket suitable for inhibitor binding **(Figure 4.2b)**. Hydrophobic interactions are often critical in stabilizing ligand binding by providing favorable van der Waals contacts and reducing solvent exposure. The 5YD4 structure further expands this network by including polar and charged residues such as Asp95, Arg97, Ile169, Asp170, Lys287, Glu288, and Glu323. These additional contacts likely modulate the electrostatic environment of the binding pocket and contribute to enhanced specificity and affinity for the particular inhibitor 5GN. These differences illustrate how both ligand chemistry and cryo-cooling conditions can influence active site conformation. Moreover, a conserved group of residues Phe96, Ile118, Ala135, Phe190, Ile232, and Val233 consistently plays a role in inhibitor binding across these structures. These residues likely serve as anchor sites which help to stabilize inhibitors within the adaptable ligand-binding pocket **(Figure 4.2a).** Minor distinctions in residue involvement between different inhibitors show the adaptability of SIRT2's binding site allowing it to accommodate chemically diverse ligands.

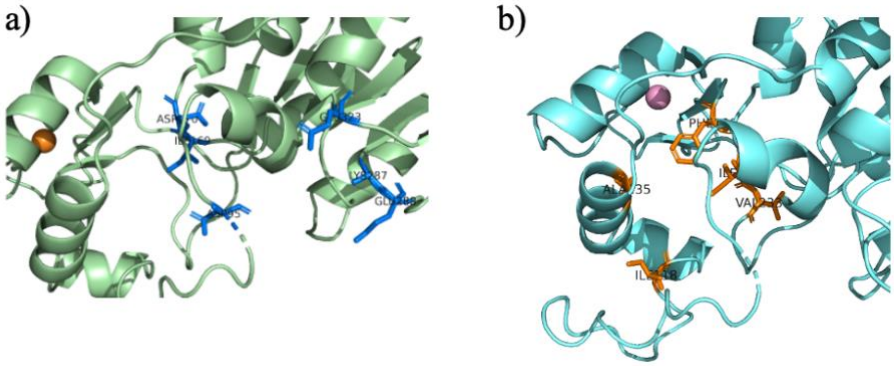

Figure 4.2: Mapping of ligand- and cofactor-interacting residues onto the ambient apo-SIRT2 structure

This figure presents a structural superposition of the ambient apo-SIRT2 (8XE7) with ligand- and cofactor-bound SIRT2 structures (5DY4 and 4RMG) to visualize cumulative conformational variability in the cofactor and ligand-binding regions. (a) Residues within 3.5 Å of NAD^+ in the 5DY4 structure Asp95, Arg97, Ile169, Asp170, Lys287, Glu288, and Glu323 are highlighted on the apo structure to indicate key cofactor-contact sites. (b) Common SirReal2-interacting residues within 3.5 Å identified in both 5DY4 and 4RMG Phe96, Ile118, Ala135, Phe190, Ile232, and Val233 are also mapped onto the apo structure. These hydrophobic, nonpolar residues define the conserved SirReal2-binding pocket and illustrate the spatial arrangement of the allosteric binding site in the ligand-free conformation.

The dynamic exchange between temperature, ligand presence, and active site conformation carries important implications. The tighter binding groove observed in the ambient temperature apo structure may better reflect SIRT2's physiological resting state before engaging with a substrate or inhibition. In contrast, ligand binding and cryo-cooling appear to stabilize a more open and accessible binding pocket, which may facilitate catalysis or inhibitor accommodation. These findings emphasize the critical role that protein flexibility and crystallization conditions that contribute shaping the enzyme's functionality and should be carefully considered in structure-based drug design strategies. Beyond these local conformational insights, broader structural features also contribute to SIRT2's regulatory mechanisms. Flexibility in regions such as the loop between Pro99 and His111, contrasted with rigidity in the Rossmann-like fold domain, highlights the complex conformational landscape of the enzyme. These features support SIRT2's status as a promising drug target due to its ability to adopt multiple conformational states relevant to its function.

Structural biology plays a crucial role in drug discovery by offering detailed molecular insights that inform the development of specific and potent inhibitors. Incorporating ambient-temperature structural data into this process enhances our understanding of target proteins in more physiologically relevant states. By revealing SIRT2's structural dynamics under near-native conditions, this study provides a strong foundation for structure-based drug design targeting this important enzyme. In conclusion, this thesis has successfully resolved the ambient-temperature apo structure of human SIRT2, offering a model that reflects the protein's native conformation. Comparative analysis with cryogenic structures reveals globally conserved folding, along with temperature and ligand-induced local conformational changes, particularly in the NAD^+ binding pocket and active site. The narrower binding groove observed at ambient temperature likely represents the enzyme's resting state, in contrast to the expanded conformations stabilized by ligand binding. Altogether, these results represents the importance of accounting for protein flexibility and experimental conditions in understanding enzyme function and improving inhibitor design.

BIBLIOGRAPHY

Ali, T. F. S., Ciftci, H. I., Radwan, M. O., Koga, R., Ohsugi, T., Okiyama, Y., Honma, T., Nakata, A., Ito, A., Yoshida, M., Fujita, M., & Otsuka, M. (2019). New SIRT2 inhibitors: Histidine-based bleomycin spin-off. Bioorganic & Medicinal Chemistry, 27(9), 1767–1775. https://doi.org/10.1016/j.bmc.2019.03.003

Arrowsmith, C.H., 2024. Structure-guided drug discovery: Back to the future. Nature Structural & Molecular Biology, 31(4), pp.395–396. https://doi.org/10.1038/s41594-024-01244-3

Atalay, N., Akcan, E.K., Gül, M., Ayan, E., Destan, E., Ertem, F.B. et al., 2023. Cryogenic X-ray crystallographic studies of biomacromolecules at Turkish Light Source "Turkish DeLight". Turkish Journal of Biology, 47(1), pp.1–13. https://doi.org/10.55730/1300-0152.2637

Chamberlain, K. A., Huang, N., Xie, Y., LiCausi, F., Li, S., Li, Y., & Sheng, Z.-H. (2021). Oligodendrocytes enhance axonal energy metabolism by deacetylation of mitochondrial proteins through transcellular delivery of SIRT2. Neuron, 109(21). https://doi.org/10.1016/j.neuron.2021.08.011

Chen, G., Huang, P., & Hu, C. (2020). The role of SIRT2 in cancer: A novel therapeutic target. International Journal of Cancer, 147(12), 3297–3304. https://doi.org/10.1002/ijc.33118

Chen, K., Wang, Y., Dai, X., Luo, J., Hu, S., Zhou, Z., Shi, J., Pan, X., Cao, T., Xia, J., Li, Y., Wang, Z., & Ma, J. (2024). FBXO31 is upregulated by METTL3 to promote pancreatic cancer progression via regulating SIRT2 ubiquitination and degradation. Cell Death and Disease, 15(1), 37. https://doi.org/10.1038/s41419-024-06425-y

Chen, K., Wang, Y., Dai, X., Luo, J., Hu, S., Zhou, Z., Shi, J., Pan, X., Cao, T., Xia, J., Li, Y., Wang, Z., & Ma, J. (2024). FBXO31 is upregulated by METTL3 to promote pancreatic cancer progression via regulating SIRT2 ubiquitination and degradation. Cell Death and Disease, 15(1), 37. https://doi.org/10.1038/s41419-024-06425-y

Chamberlain, K. A., Huang, N., Xie, Y., LiCausi, F., Li, S., Li, Y., & Sheng, Z.-H. (2021). Oligodendrocytes enhance axonal energy metabolism by deacetylation of mitochondrial proteins through transcellular delivery of SIRT2. Neuron, 109(21). https://doi.org/10.1016/j.neuron.2021.08.011

Dludla, P. V., Mabhida, S. E., Ziqubu, K., Nkambule, B. B., Mazibuko-Mbeje, S. E., Hanser, S., Basson, A. K., Pheiffer, C., & Kengne, A. P. (2023a). Pancreatic β-cell dysfunction in type 2 diabetes: Implications of inflammation and oxidative stress. World Journal of Diabetes, 14(3), 130–146. https://doi.org/10.4239/wjd.v14.i3.130

Ensembl, 2024. SIRT2 gene: Homo sapiens. [online] Ensembl Genome Browser. Available at: https://www.ensembl.org
Finnin, M. S., Donigian, J. R., & Pavletich, N. P. (2001). Structure of the histone deacetylase SIRT2 bound to its cofactor NAD+ and an inhibitor. Nature Structural Biology, 8(7), 621–625. https://doi.org/10.1038/89668

Funato, K., Hayashi, T., Echizen, K., Negishi, L., Shimizu, N., Koyama-Nasu, R., Nasu-Nishimura, Y., Morishita, Y., Tabar, V., Todo, T., Ino, Y., Mukasa, A., Saito, N., & Akiyama, T. (2018). SIRT2-mediated inactivation of p73 is required for glioblastoma tumorigenicity. EMBO Reports, 19(11). https://doi.org/10.15252/embr.201745587

Garmendia-Berges, M., Sola-Sevilla, N., Mera-Delgado, Mc., & Puerta, E. (2023). Age-associated changes of SIRTUIN 2 expression in CNS and the periphery. Biology, 12(12), 1476. https://doi.org/10.3390/biology12121476

GenScript. (t.y.). pET-28a(+) bacterial expression vector map [PDF]. https://www.genscript.com/gsfiles/vector-map/bacteria/pET-28a.pdf

Hamaidi, I., Zhang, L., Kim, N., Wang, M.-H., Iclozan, C., Fang, B., Liu, M., Koomen, J. M., Berglund, A. E., Yoder, S. J., Yao, J., Engelman, R. W., Creelan, B. C., Conejo-Garcia, J. R., Antonia, S. J., Mulé, J. J., & Kim, S. (2020). SIRT2 inhibition enhances metabolic fitness and effector functions of tumor-reactive T cells. Cell Metabolism, 32(3). https://doi.org/10.1016/j.cmet.2020.07.008

Houtkooper, R. H., Pirinen, E., & Auwerx, J. (2012). Sirtuins as regulators of metabolism and healthspan. Nature Reviews Molecular Cell Biology, 13(4), 225–238. https://doi.org/10.1038/nrm3293

Hu, J., Jing, H., & Lin, H. (2014). Sirtuin inhibitors as Anticancer Agents. Future Medicinal Chemistry, 6(8), 945–966. https://doi.org/10.4155/fmc.14.44

Huang, S., Song, C., Wang, X., Zhang, G., Wang, Y., Jiang, X., Sun, Q., Huang, L., Xiang, R., Hu, Y., Li, L., & Yang, S. (2017). Discovery of New SIRT2 Inhibitors by Utilizing a Consensus Docking/Scoring Strategy and Structure-Activity Relationship Analysis. Journal of chemical information and modeling, 57(4), 669–679. https://doi.org/10.1021/acs.jcim.6b00714

Huang, H. L., Jiang, Y., Wang, Y. H., Chen, T., He, H. J., Liu, T., Yang, T., Yang, L. W., Chen, J., Song, Z. Q., Yao, W., Wu, B., & Liu, G. (2015). FBXO31 promotes cell proliferation, metastasis and invasion in lung cancer. American Journal of Cancer Research, 5(5), 1814–1822.

Isohookana, J., Haapasaari, K. M., Soini, Y., & Karihtala, P. (2018). KDM4D Predicts Recurrence in Exocrine Pancreatic Cells of Resection Margins from Patients with Pancreatic Adenocarcinoma. Anticancer Research, 38(4), 2295–2302. https://doi.org/10.21873/anticanres.12474

Jumper, J., Evans, R., Pritzel, A., Green, T., Figurnov, M., Ronneberger, O., Tunyasuvunakool, K., Bates, R., Žídek, A., Potapenko, A., Bridgland, A., Meyer, C., Kohl, S. A., Ballard, A. J., Cowie, A., Romera-Paredes, B., Nikolov, S., Jain, R., Adler, J., … Hassabis, D. (2021). Highly accurate protein structure prediction with alphafold. Nature, 596(7873), 583–589. https://doi.org/10.1038/s41586-021-03819-2

Kudo, N., Ito, A., Arata, M., Nakata, A., & Yoshida, M. (2018). Identification of a novel small molecule that inhibits deacetylase but not defatty-acylase reaction catalysed by SIRT2. Philosophical Transactions of the Royal Society B: Biological Sciences, 373(1748), 20170070. https://doi.org/10.1098/rstb.2017.0070

Kunadis, E., Lakiotaki, E., Korkolopoulou, P., & Piperi, C. (2021). Targeting post-translational histone modifying enzymes in glioblastoma. Pharmacology & Therapeutics, 220, 107721. https://doi.org/10.1016/j.pharmthera.2020.107721

Li, N., Bai, N., Zhao, X., Cheng, R., Wu, X., Jiang, B., Li, X., Xue, M., Xu, H., Guo, Q., Guo, W., Ma, M., Cao, S., Feng, Y., Song, X., Wang, Z., Zhang, X., Zou, Y., Wang, D., … Cao, L. (2023). Cooperative effects of SIRT1 and SIRT2 on APP acetylation. Aging Cell, 22(10). https://doi.org/10.1111/acel.13967

Li, B., Hong, P., Zheng, C. C., Dai, W., Chen, W. Y., Yang, Q. S., ... & Cheung, A. L. (2019). Identification of miR-29c and its Target FBXO31 as a Key Regulatory Mechanism in Esophageal Cancer Chemoresistance: Functional Validation and Clinical Significance. Theranostics, 9(6), 1599–1613. https://doi.org/10.7150/thno.30372

Liu, J., Lv, L., Gong, J., Tan, Y., Zhu, Y., Dai, Y., ... & Cheung, A. L. M. (2018). Overexpression of F-box only protein 31 predicts poor prognosis and deregulates p38α- and JNK-mediated apoptosis in esophageal squamous cell carcinoma. International Journal of Cancer, 142(1), 145–155. https://doi.org/10.1002/ijc.31040

Liu, P. Y., Xu, N., Malyukova, A., Scarlett, C. J., Sun, Y. T., Zhang, X. D., ... & Liu, T. (2013). The histone deacetylase SIRT2 stabilizes Myc oncoproteins. Cell Death & Differentiation, 20(3), 503–514. https://doi.org/10.1038/cdd.2012.147

Lu, W., Ji, H., & Wu, D. (2023). SIRT2 plays complex roles in neuroinflammation neuroimmunology-associated disorders. Frontiers in Immunology, 14. https://doi.org/10.3389/fimmu.2023.1174180

Manjula, R., Anuja, K., & Alcain, F. J. (2021). SIRT1 and SIRT2 activity control in neurodegenerative diseases. Frontiers in Pharmacology, 11. https://doi.org/10.3389/fphar.2020.585821

Malgulwar, P. B., Danussi, C., Dharmaiah, S., Johnson, W., Singh, A., Rai, K., Rao, A., & Huse, J. T. (2023). Sirtuin 2 inhibition modulates chromatin landscapes genome-wide to induce senescence in ATRX-deficient malignant glioma. Neuro-Oncology, 26(1), 55–67. https://doi.org/10.1093/neuonc/noad155

McPherson, A., & Gavira, J. A. (2013). Introduction to protein crystallization. Acta Crystallographica Section F Structural Biology Communications, 70(1), 2–20. https://doi.org/10.1107/s2053230x13033141

Michishita, E., Park, J. Y., Burneskis, J. M., Barrett, J. C., & Horikawa, I. (2005). Evolutionarily conserved and nonconserved cellular localizations and functions of human SIRT proteins. Molecular Biology of the Cell, 16(10), 4623–4635. https://doi.org/10.1091/mbc.e05-01-0033
Minten, E. V., Kapoor-Vazirani, P., Li, C., Zhang, H., Balakrishnan, K., & Yu, D. S. (2021). SIRT2 promotes BRCA1-Bard1 heterodimerization through deacetylation. Cell Reports, 34(13), 108921. https://doi.org/10.1016/j.celrep.2021.108921

North, B. J., Rosenberg, M. A., Jeganathan, K. B., Hafner, A. V., Michan, S., Dai, J., Baker, D. J., Cen, Y., Wu, L. E., Sauve, A. A., van Deursen, J. M., Rosenzweig, A., & Sinclair, D. A. (2014). SIRT2 induces the checkpoint kinase BUBR1 to increase lifespan. The EMBO Journal, 33(13), 1438–1453. https://doi.org/10.15252/embj.201386907

Quan, S., Principe, D. R., Dean, A. E., Park, S. H., Grippo, P. J., Gius, D., & Horikoshi, N. (2018). Loss of Sirt2 increases and prolongs a caerulein-induced pancreatitis permissive phenotype and induces spontaneous oncogenic Kras mutations in mice. Scientific Reports, 8(1), 16501. https://doi.org/10.1038/s41598-018-34792-y

Radwan, M. O., Ciftci, H. I., Ali, T. F. S., Koga, R., Tateishi, H., Nakata, A., Ito, A., Yoshida, M., Fujita, M., & Otsuka, M. (2020). Structure activity study of S-trityl-cysteamine dimethylaminopyridine derivatives as SIRT2 inhibitors: Improvement of SIRT2 binding and inhibition. Bioorganic & Medicinal Chemistry Letters, 30(19), 127458. https://doi.org/10.1016/j.bmcl.2020.127458

Ramakrishnan, G., Davaakhuu, G., Kaplun, L., Chung, W.-C., Rana, A., Atfi, A., Miele, L., & Tzivion, G. (2014). SIRT2 deacetylase is a novel Akt binding partner critical for AKT activation by insulin. Journal of Biological Chemistry, 289(9), 6054–6066. https://doi.org/10.1074/jbc.m113.537266

Rosano, G. L., & Ceccarelli, E. A. (2014a). Recombinant protein expression in escherichia coli: Advances and challenges. Frontiers in Microbiology, 5. https://doi.org/10.3389/fmicb.2014.00172

Roshdy, E., Mustafa, M., Shaltout, A. E.-R., Radwan, M. O., Ibrahim, M. A. A., Soliman, M. E., Fujita, M., Otsuka, M., & Ali, T. F. S. (2021). Selective SIRT2 inhibitors as promising anticancer therapeutics: An update from 2016 to 2020. European Journal of Medicinal Chemistry, 224, 113709. https://doi.org/10.1016/j.ejmech.2021.113709

Santra, M. K., Wajapeyee, N., & Green, M. R. (2009). F-box protein FBXO31 mediates cyclin D1 degradation to induce G1 arrest after DNA damage. Nature, 459(7247), 722–725. https://doi.org/10.1038/nature08011

Sarikhani, M., Mishra, S., Desingu, P. A., Kotyada, C., Wolfgeher, D., Gupta, M. P., Singh, M., & Sundaresan, N. R. (2018). SIRT2 regulates oxidative stress-induced cell death through deacetylation of c-jun NH2-terminal kinase. Cell Death & Differentiation, 25(9), 1638–1656. https://doi.org/10.1038/s41418-018-0069-8

Senft, D., Qi, J., & Ronai, Z. A. (2018). Ubiquitin ligases in oncogenic transformation and cancer therapy. Nature Reviews Cancer, 18(2), 69–88. https://doi.org/10.1038/nrc.2017.105

Skaar, J. R., Pagan, J. K., & Pagano, M. (2013). Mechanisms and function of substrate recruitment by F-box proteins. Nature reviews. Molecular cell biology, 14(6), 369–381. https://doi.org/10.1038/nrm3582

Smyth, M. S. (2000). X ray crystallography. Molecular Pathology, 53(1), 8–14. https://doi.org/10.1136/mp.53.1.8

Sola-Sevilla, N., Mesa-Lombardo, A., Aleixo, M., Expósito, S., Diaz-Perdigón, T., Azqueta, A., Zamani, F., Suzuki, T., Maioli, S., Eroli, F., Matton, A., Ramírez, M. J., Solas, M., Tordera, R. M., Martín, E. D., & Puerta, E. (2023). SIRT2 inhibition rescues neurodegenerative pathology but increases systemic inflammation in a transgenic mouse model of Alzheimer's disease. Journal of Neuroimmune Pharmacology, 18(3), 529–550. https://doi.org/10.1007/s11481-023-10084-9

Song, H. Y., Biancucci, M., Kang, H. J., O'Callaghan, C., Park, S. H., Principe, D. R., ... & Vassilopoulos, A. (2016). SIRT2 deletion enhances KRAS-induced tumorigenesis in vivo by regulating K147 acetylation status. Oncotarget, 7(49), 80336. https://doi.org/10.18632/oncotarget.12015

Spiegelman, N. A., Price, I. R., Jing, H., Wang, M., Yang, M., Cao, J., ... & Lin, H. (2018). Direct comparison of SIRT2 inhibitors: Potency, specificity, activity-dependent inhibition, and on-target anticancer activities. ChemMedChem. https://www.ncbi.nlm.nih.gov/pmc/articles/PMC6402572/

Tailor, B., Pilozzi, A., & Huang, X. (2019). Contributing factors of neurodegeneration in Alzheimer's disease. In Alzheimer's Disease (pp. 69–84). https://doi.org/10.15586/alzheimersdisease.2019.ch5

Turcan, Ş. (2023). SIRT2 inhibition as the Achilles' heel of ATRX-deficient gliomas. Neuro-Oncology, 26(1), 68–69. https://doi.org/10.1093/neuonc/noad217

Wang, Y., Yang, J., Hong, T., Chen, X., & Cui, L. (2019). Sirt2: Controversy and multiple roles in disease and physiology. Ageing Research Reviews, 55, 100961. https://doi.org/10.1016/j.arr.2019.100961

Wan, Y., Wu, W., Zhang, J., Li, L., Wan, Y., Tang, X., Chen, X., Liu, S., & Yao, X. (2021). Tenovin-1 inhibited dengue virus replication through SIRT2. European Journal of Pharmacology, 907, 174264. https://doi.org/10.1016/j.ejphar.2021.174264

Wlodawer, A., & Vondrasek, J. (1998). Inhibitors of HIV-1 protease: A major success of structure-assisted drug design. Annual Review of Biophysics and Biomolecular Structure, 27(1), 249–284. https://doi.org/10.1146/annurev.biophys.27.1.249

Wu, Q.-J., Zhang, T.-N., Chen, H.-H., Yu, X.-F., Lv, J.-L., Liu, Y.-Y., ... & Zhao, Y.-H. (2022). The sirtuin family in health and disease. Signal Transduction and Targeted Therapy, 7(1). https://doi.org/10.1038/s41392-022-01257-8

Yang, J., Wang, H., Liu, J., Ma, E., Jin, X., Li, Y., & Ma, C. (2024). Screening approach by a combination of computational and in vitro experiments: Identification of fluvastatin sodium as a potential SIRT2 inhibitor. Journal of Molecular Modeling, 30(6), 188. https://doi.org/10.1007/s00894-024-05988-z

Yu, L., Li, Y., Song, S., Zhang, Y., Wang, Y., Wang, H., Yang, Z., & Wang, Y. (2024). The dual role of sirtuins in cancer: Biological functions and implications. Frontiers in Oncology, 14. https://doi.org/10.3389/fonc.2024.1384928

Zhang, L., Kim, S., & Ren, X. (2020). The clinical significance of SIRT2 in malignancies: A tumor suppressor or an oncogene? Frontiers in Oncology, 10. https://doi.org/10.3389/fonc.2020.01721

Zhang, Y., Wang, X., Li, X.-K., Lv, S.-J., Wang, H.-P., Liu, Y., Zhou, J., Gong, H., Chen, X.-F., Ren, S.-C., Zhang, H., Dai, Y., Cai, H., Yan, B., Chen, H.-Z., & Tang, X. (2023, August 1). SIRTUIN 2 deficiency aggravates ageing-induced vascular remodelling in humans and mice. European heart journal. https://pmc.ncbi.nlm.nih.gov/articles/PMC10393077/

Zhou, C., Jung, C.-G., Kim, M.-J., Watanabe, A., Abdelhamid, M., Taslima, F., & Michikawa, M. (2022). Insulin deficiency increases SIRT2 level in streptozotocin-treated alzheimer's disease-like mouse model: Increased SIRT2 induces tau phosphorylation through Erk Activation. Molecular Neurobiology, 59(9), 5408–5425. https://doi.org/10.1007/s12035-022-02918-z

Zhao, D., Zou, S. W., Liu, Y., Zhou, X., Mo, Y., Wang, P., ... & Guan, K. L. (2013). Lysine-5 acetylation negatively regulates lactate dehydrogenase A and is decreased in pancreatic cancer. Cancer Cell, 23(4), 464–476. https://doi.org/10.1016/j.ccr.2013.02.005

Zhu, C., Dong, X., Wang, X., Zheng, Y., Qiu, J., Peng, Y., Xu, J., Chai, Z., & Liu, C. (2022). Multiple roles of SIRT2 in regulating physiological and pathological signal transduction. Genetics Research, 2022, 1–14. https://doi.org/10.1155/2022/9282484

APPENDIX A: CHEMICALS

Chemical	**Supplier Company**
Acetic Acid	ISOLAB
Acrylamide/Bis-acrylamide	Bio-Rad
APS	Sigma-Aldrich
Chloramphenicol	GOLDBIO
Coomassie Brilliant Blue	Bio-Rad
Ethanol	ISOLAB
Glycerol	ISOLAB
Glycine	ISOLAB
HCl	ISOLAB
Imidazole	Biofroxx
IPTG	GOLDBIO
Kanamycin	GOLDBIO
LB	Thermo Fisher
LB Agar	Sigma-Aldrich
Lysozyme	Caisson
NaCl	ISOLAB
NaOH	ISOLAB
Ni-NTA Resin	QIAGEN
Paraffin Oil	TEKKİM
SDS	ISOLAB
TEMED	Sigma-Aldrich
Tris-HCl	Sigma-Aldrich
Triton X-100	Sigma-Aldrich
Tryptone	BD Biosciences
Yeast Extract	BD Biosciences

APPENDIX B: EQUIPMENTS

Chemical	**Supplier Company**
Acetic Acid	ISOLAB
Acrylamide/Bis-acrylamide	Bio-Rad
APS	Sigma-Aldrich
BME	Merck
Chloramphenicol	GOLDBIO
Coomassie Brilliant Blue	Bio-Rad
DTT	Roche
Ethanol	ISOLAB
Glycerol	ISOLAB
Glycine	ISOLAB
HCl	ISOLAB
Imidazole	Biofroxx
IPTG	GOLDBIO
Kanamycin	GOLDBIO
LB	Thermo Fisher
LB Agar	Sigma-Aldrich
Lysozyme	Caisson
NaCl	ISOLAB
NaOH	ISOLAB
Ni-NTA Resin	QIAGEN
Paraffin Oil	TEKKİM
PMSF	GOLDBIO
SDS	ISOLAB
TEMED	Sigma-Aldrich
Thrombin Protease	Sigma-Aldrich
Tris-HCl	Sigma-Aldrich
Triton X-100	Sigma-Aldrich
Tryptone	BD Biosciences
Yeast Extract	BD Biosciences

APPENDIX C: CRYSTALLIZATION SCREENS

Crystallization Screen	**Supplier Company**
3D Structure Screen	Molecular Dimensions
Additive Screen	Hampton Research
Clear Strategy Screen	Molecular Dimensions
CryoPro	Hampton Research
Crystal Screen	Hampton Research
Crystal Screen Cryo	Hampton Research
Detergent Screen	Hampton Research
Grid Screen Ammonium Sulfate	Hampton Research
Grid Screen MPD	Hampton Research
Grid Screen PEG/LiCl	Hampton Research
Grid Screen PEG6000	Hampton Research
Grid Screen Sodium Chloride	Hampton Research
Helix	Molecular Dimensions
Index	Hampton Research
Ionic Liquid Screen	Hampton Research
JBScreen Nuc-Pro	Jena Bioscience
JCSG	Molecular Dimensions
MacroSol	Molecular Dimensions
MembFac	Hampton Research
MIDAS	Molecular Dimensions
Morpheus	Molecular Dimensions
MultiXtal	Molecular Dimensions
Natrix	Hampton Research
NeXtal Protein Complex Suite	NeXtal Biotechnologies
NR-LBD	Molecular Dimensions
PACT Premier	Molecular Dimensions
PEG/Ion	Hampton Research
PEGRx	Hampton Research
PGA Screen	Molecular Dimensions
ProPlex Screen	Molecular Dimensions
Quick Screen	Hampton Research
SaltRx	Hampton Research
Structure Screen	Molecular Dimensions
Stura FootPrint Screen	Molecular Dimensions
Wizard	Rigaku

Crystallization Screen	**Supplier Company**
Wizard Cryo	Rigaku
Wizard Precipitant Synergy	Rigaku